Development of an Occupant and Vehicle Interaction Simulation

Except where reference is made to the work of others, the work described in this thesis is my own or was done in collaboration with my advisory committee. This thesis does not include proprietary or classified information.

_____
Marc Jarmulowicz

Certificate of Approval:

_____   _____
Peter D. Jones   Winfred A. Foster Jr., Chair
Associate Professor   Professor
Mechanical Engineering   Aerospace Engineering

_____   _____
Nels H. Madsen   George T. Flowers
Associate Dean for Assessment & Special   Interim Dean, Graduate School
Programs
Mechanical Engineering

DEVELOPMENT OF AN OCCUPANT AND VEHICLE INTERACTION SIMULATION

Marc Jarmulowicz

A Thesis

Submitted to

the Graduate Faculty of

Auburn University

in Partial Fulfillment of the

Requirements for the

Degree of

Master of Science

Auburn, Alabama
December 17, 2007

Development of an Occupant and Vehicle Interaction Simulation

Marc Jarmulowicz

_____

Signature of Author

_____

Date of Graduation

Vita

Marc Daniel Jarmulowicz, son of Wesley and Mary Ann Jarmulowicz was born October 20, 1983 in Long Beach, California. In 2001, he graduated from Beaufort Academy, in Beaufort, SC. He attended Auburn University in 2001 and graduated with a Bachelors of Science degree in Aerospace Engineering in 2005. In 2005 he began graduate school in the Aerospace Engineering Department at Auburn University and received his Masters of Science in 2007.

Thesis Abstract

Development of an Occupant and Vehicle Interaction Simulation

Marc Jarmulowicz

Master of Science, December 17, 2007
(B.S., Auburn University, 2005)

118 Typed Pages

Directed by Winfred A. Foster Jr.

The focus of this thesis was on performing a non-linear, transient occupant and structure interaction simulation. A finite element model was created of the Auburn University 2005 Baja SAE vehicle in combination with an occupant model. The objective of this work was to develop and verify this model for structural interaction with occupant kinematics. The work consisted of obtaining experimental data from tests and comparing them with a computer simulation. The results of the simulation showed that the model gave an adequate reproduction of low speed impacts, and was useful in simulating the effects of transferring externally applied loads to the vehicle and in turn, to the occupant.

Style manual or journal used Journal of Approximation Theory (together with the style known as "aums"). Bibliography follows van Leunen's *A Handbook for Scholars.*

Computer software used The document preparation package TeX (specifically LaTeX) together with the departmental style-file `aums.sty`.

xiii

Introduction

The design of an off-road race vehicle is unique among motor sports vehicles. The design of such a vehicle is often viewed to be less sophisticated in comparison to a Formula one race car, when in reality the simplicity of construction makes the vehicle more robust. Very often drivers in off-road race cars will damage their vehicles, proceed to fix the damage, and continue on. As such, the vehicle as a whole must be damage-tolerant under a wide range of conditions, including roll-overs. Roll-overs is a term used to describe a vehicle rotating end over end or on its side, and in this type of accident the loads are unknown, and difficult to obtain with data acquisition equipment. This example is juxtaposed to a Formula One vehicle accident, where the design loads are often in the plane of travel, or with no roll-overs. Furthermore, the design of the off-road vehicle lends itself to be easily simulated on the computer. Due to the need for a robust and damage tolerant structure, the frames of these vehicles are space-frames where tubes of steel alloys make up a webbing through which all the loads on the vehicle are transfered. The space-frame is ideal to model in a finite element solution with beam elements, and provides a convenient method to attach all of the vehicle substructures, including occupants.

Very little work has been done to incorporate occupant simulations into off-road vehicle simulations, but the simplicity of the vehicle allows a single simulation to do occupant dynamics, vehicle dynamics, frame stress and loads analysis. Coupling the explicit transient solution capabilities in MSC.Dytran [12], with the kinematics solver of the Articulated

Total Body (ATB) [7] simulation, and with the human database of the Generator of Body Data (GEBOD) [14] computer program, provides the ability to do just such a simulation. MSC.Dytran is used to build the finite element vehicle frame, and solves the stiffness matrices as well as the contact between arbitrary surfaces and the frame. This simulation also calculates seatbelt motion and forces. The ATB program calculates the motion of ellipsoids with mass and volume in relation to joints of many types. These joints may represent pin joints in one direction or Euler joints with motion in all directions. The mass for all of the ellipsoids and the joint stiffness data all come from the GEBOD program, which interpolates human body data from Air Force research. The goal of the work presented is to apply a known force to a Baja SAE vehicle and compare the response of the experimental occupant to that of the simulated occupant, specifically though the load in the seat belts. The ability to apply a known force allows for stress analysis in what would normally be a rigid body dynamics analysis. It is possible to simulate the stress distribution in a frame of a vehicle as it encounters an obstacle, with known suspension loads for that obstacle. Since the simulation is a free body in space, this presents an opportunity to analyze overall vehicle dynamics. Due to the simplicity that off-road vehicles inherently have in their tube structure, single simulations can be run to obtain data that would normally come from different programs.

Background into the development of off-road vehicle finite element analysis is presented in chapter 2. A review of applicable literature to accident dynamics is presented in chapter 3. Detail of the development of the computer simulation is explained in chapter 4. The methodology and theory for verifying the simulation presented matches the experimental

results is described in chapter 5. The results of the simulation compared to the experiment along with an explanation of those results are presented in chapter 6, and the conclusions developed from the overall work are presented in chapter 7.

Background

This research is based on the usage of a particular vehicle, known as a Baja SAE vehicle, shown in Figure 2.1. The Baja SAE vehicle is used in the collegiate racing series offered by the Society of Automotive Engineers. In this racing series, college students design and build vehicles to compete against each other in specific tasks. Examples of these tasks are events to compare the top speed, the maneuverability, or the robustness of the design. The general layout of a Baja SAE car is a steel alloy tube space frame vehicle, whose driver sits in front of an engine and drive-train, with a bulkhead called a firewall in between. The maximum speed of such a vehicle is around 35 mph.

Figure 2.1: 2005 Auburn Baja SAE Vehicle

The competition's most demanding task is an endurance race, where the vehicles race wheel to wheel over an off-road track that under normal conditions is impassable to all vehicles except to All-Terrain Vehicles or ATVs. It is common for the vehicles in this race to

overturn on their side and impact the ground in ways that the suspension cannot dissipate any energy from such an impact. The resulting loads from this type of impact are unknown. Without this load history, the frame of the vehicle is designed to assumed maximum loads since actual values are not typically available. The assumed loads are large in magnitude so that a factor of safety is built into the design, but how large a safety factor is unknown.

Simulating the response of the Baja SAE vehicle to different load cases is accomplished by several methods. In considering the methods in which a finite element model can be used, there are two types of analysis, static and dynamic, that can be used to determine the stress in the frame. In a static analysis the forces are applied to a node of the model and these forces are reacted at points which are constrained. The points which are constrained make up a part of a set known as the boundary conditions, this set can incorporate many different effects depending on the type of linear simulation. In general, the static analysis is defined by Equation 2.1, where f represents a column of applied forces, K is a matrix with stiffness terms of all degrees of freedom, and d is a column vector which represents enforced displacements to the model.

$$\{f\} = [K] \{d\} \tag{2.1}$$

In finite element terms, boundary conditions are locations of prescribed movement, and are represented by removing columns or rows corresponding to specific degrees of freedom out of the f and d vectors and the [K] matrix [17]. In a static solution, if a force is applied, a boundary condition must be applied as well. Thus the problem in representing a vehicle event like jumping becomes a choice of boundary conditions to represent a dynamic event

with a static solution. The vehicle frames are often designed to repeatedly withstand a so-called single wheel jumping load, which represents a worst case scenario in which twice the total weight of the vehicle is applied at one shock absorber attachment point. A common boundary condition for this scenario is to constrain the motion of the firewall. If another boundary condition was chosen, like constraining the motion of the seat (the location where the occupants mass has a great dynamic effect), the applied loads would have to be symmetric across all the shock points. If the applied loads are not symmetric, unrealistic stresses and deformations will result from the seat being loaded in bending, which with an occupant is not a way that it can be physically loaded. With these inherent problems, the dynamic solution becomes the next step in a more accurate solution.

A dynamic solution, also called a transient solution since it is time-dependent, involves solving the equations of motion for a structure to determine the motion of the structure in spaces as well as the resulting stresses in such a structure. The general form of the equation of motion is shown in Equation 2.2.

$$[M]\frac{d^2}{dx^2}\{x\} + [C]\frac{d}{dx}\{x\} + [K]\{x\} = \{f\} \tag{2.2}$$

In Equation 2.2, [M] represents the mass for the model, [C] represents the dampening matrix, and [K] represents the stiffness matrix. For each of these terms, there is an $\{x\}$, $\frac{d}{dx}\{x\}$, or $\frac{d^2}{dx^2}\{x\}$ vector which resolves into a force. Mass times acceleration, damping times velocity, and spring stiffness times position all resolve into forces. The mass matrix can be represented as lumped or coupled, the differences being that a lumped mass matrix places all the mass of an element at its nodes, while a coupled mass matrix assumes that

6

there is coupling between the translational degrees of freedom and the rotational ones. As such, a lumped mass matrix is diagonal and easier to compute, where a coupled mass matrix is full and more difficult to compute since its equations are not linearly independent [15].

The dynamic solution comes in many types, two of which are linear and non-linear. A linear solution is computationally easier since the geometry of the model is unchanged due to the load applied. A non-linear solution changes the stiffness and mass matrices, which allow for the geometry to move in the direction of the loading and also allows for non-linear material effects like plastic deformation. Plastic deformation is permanent deformation of a structure due to an applied load. In modeling a dynamic event, boundary conditions can be applied to constrain the motion of the model, but are not a requirement. Unlike a static model which may have unrealistic boundary conditions, a dynamic model can be very realistic assuming the mass is properly represented and the force is applied in a reasonable fashion. For vehicles like the Baja SAE vehicle, a major problem still remains in modeling the effects of the human body. The total weight for the Baja SAE vehicle and occupant used in this work was 288 kg (635 lbs); the occupant's weight made up 113 kg (250 lbs) of the total weight. Thus the occupant represents roughly one third of the total mass, and so it is not negligible. The mass of the occupant can be represented in a number of different ways, one of them with the body idealized into a point mass and another with the body represented as segments free to move in space. Representing the occupant as a point mass cannot represent the dynamic behavior of the human body, and has an inherent problem of attaching the mass to the vehicle. Even though it is possible to connect a point mass to the larger structure using only the translational degrees of freedom, the geometry of the model

will still create bending moments where there should be none. An example of this problem can be visualized if a point mass is connected to a seat model; due to the seat being two dimensional, the length and width of the seat create moment arms in attaching the point mass. However, in reality the seat can transmit no rotation to the body, only normal forces. Using the Articulated Total Body simulation allows the mass and dynamic properties of the human body to interact with a finite element structure in a free dynamic environment, using computational contacts between objects in a model. These contacts allow for normal and in-plane forces to be developed in the seat, but do not transfer rotations directly.

2.1 The Value of An Occupant and Vehicle Interaction Simulation

The advantages to the proposed model are that the geometry and physics can be captured with high fidelity, and the occupant response can be determined. Since the vehicle represented in this simulation is relatively simple, the finite element model can have high fidelity with relatively few elements. This high fidelity allows for the occupant model to interact with the vehicle model in a way that gives a good approximation of reality. The occupant is constrained to the vehicle through the seat and the seat belts, which apply normal forces like pressures and tangential forces like friction. These are the only two types of forces that are applied to the occupant, and other modeling techniques may introduce bending moments where there should be none. This simulation is also more accurate due to the ability to model non-linear structural dynamics such as changes in geometry. The human body response allows for determination of body accelerations and HIC loads [7].

Potential problems with this simulation stem from modeling the occupant and the

contact between the occupant and the vehicle. The occupant is modeled in a way that assumes that the joints are torsional springs, and that there is no active control of the body. Both of these assumptions have a significant effect on the dynamic response of the occupant. The contact routines between the occupant and the vehicle use assumed friction coefficients and contact parameters such as penetration depth. The MSC.Dytran solver updates the geometry of the stiffness matrix in response to loads, as in a non-linear analysis. In this way the seat belt elements are allowed to conform to the occupant so that the simulation determines the geometry of the belts and how they contact the body. The frame geometry is also updated as the solution progresses, but the loads used in the validation of this model do not create plastic deformations in the structure of the frame.

The practical value of this simulation is the application of known load data that allows for detailed structural analysis. This analysis can lead to results such as a reduction in weight of the space frame, while maintaining reliability. In the case of structural failure, a simulation could be developed to analyze the effect of the vehicle impacting a tree. This simulation environment allows for the flexibility to give initial conditions about the tree and the vehicle and allow the computer to determine the applied loads. This ability is very useful for a majority of problems where the type of contact the initial conditions may be known, but the actual forces are not known. In this way, the model proposed in this work allows for a level of analysis previously not performed in the Baja SAE racing community.

CHAPTER 3

REVIEW OF EARLIER DYNAMIC SIMULATIONS

Much of the past work done in off road vehicle simulation has been documented in engineering journals like those from the Society of Automotive Engineers. The first documented dynamic simulation of a Baja SAE car was from da Silva et al. [16]. Their work focused on verifying a two degree of freedom simulation in a MATLAB environment. The theory of their two degree of freedom model is shown in Figure 3.1 (b). Their experiment consisted of driving a Baja SAE vehicle over an instrumented object as seen in Figure 3.1 (d). In this experiment both the obstacle and the vehicle were instrumented with load cells as shown in Figures 3.1 (a) and (c). Due to the sinusoidal shape of the obstacle and the theoretical requirement that the tires never loose contact with the obstacle, the speed of the vehicle was limited to less than 2.0 m/s (4.5 mph). They determined that for low speed conditions, a two degree of freedom model adequately matched the available data as seen in Figure 3.2. They proposed that their model could be used to study the suspension system performance and to modify it for pilot comfort [16].

Investigation into computer simulations to reproduce dynamic simulations was continued in the work by Owens et al. [13]. In this work a dynamic simulation of a Baja SAE vehicle was made after verifying the frame finite element model with both a static and a modal analysis. All simulations were run in the ABAQUS finite element environment. The static analysis of the Baja SAE frame involved applying a known torque to the frame with known constraints as shown in Figure 3.3. The static simulation produced good results,

10

(a)
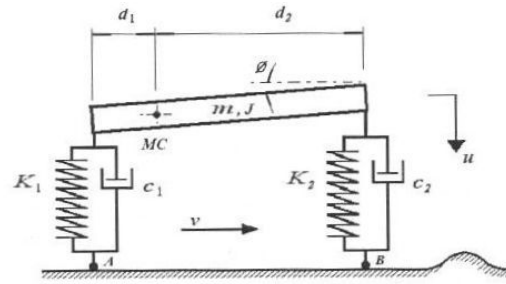
(b)

(c)

(d)

Figure 3.1: Early Baja SAE experimentation, obstacle (a), theoretical model (b), vehicle (c), and experiment (d) - Source: [16].
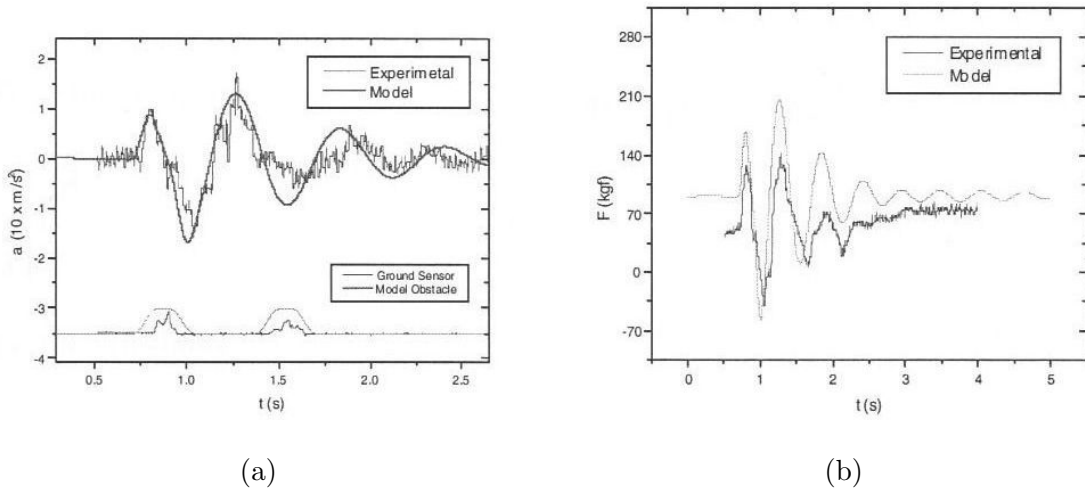
Figure 3.2: Results from MATLAB simulation, vehicle accelerations (a) and loads (b) - Source: [16].

and the torsional rigidity of the frame was found to be within 8% of the simulation [13]. Torsional rigidity is the spring rate of the frame if one end is twisted and the other is constrained. For the modal analysis, the frame was constrained to a rigid table and impacted. A full spectrum of frequencies from two accelerometer locations were recorded. The modal experimentation procedure presented in [13] was the basis for the procedure used to verify occupant and vehicle simulation.

The dynamic model that was constructed in [13] is based on the model that they validated in their static and modal analyses. This model had a high fidelity frame model, and incorporated a point mass occupant representation. The point mass was connected to several nodes on the frame that represented the seat attachment locations and harness attachment locations. To represent the inertia of the vehicle as a whole, correction masses and inertias were added to the frame model. They concluded that the simulated stresses

12
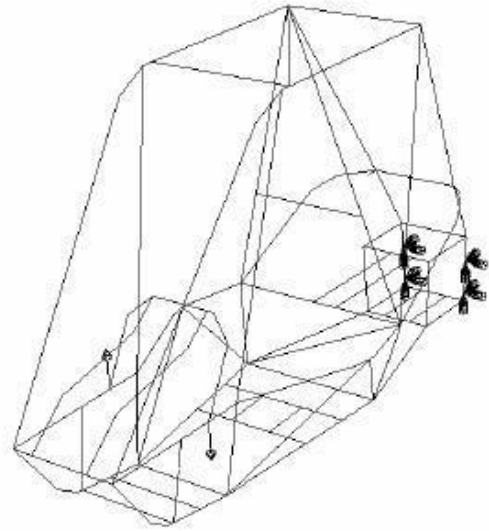
(a)   (b)

Figure 3.3: Static displacement test experiment (a), and simulation (b) - Source: [13].

were high in magnitude for an applied loading in a place that did not see fatigue failure.

The Articulated Total Body simulation has many documented verification tests to prove its capability. In the one of these tests, Smith et al. [18] simulated two different rollover events for the same type of minivan. Called a developmental test, the first rollover was of a 1988 Dodge Caravan. The rollover was initiated by a rollover test device, which gave the minivan an initial velocity of 48.3 kph (30 mph) before flipping it. In this case, the minivan landed on its left side and slid on its left side. Video from inside the vehicle was compared with results from the gross body motion of the simulation, and seemed to agree well. The plots of the acceleration are shown as well, and seem to exhibit good trends, but have unknown asymptotic peaks.

13
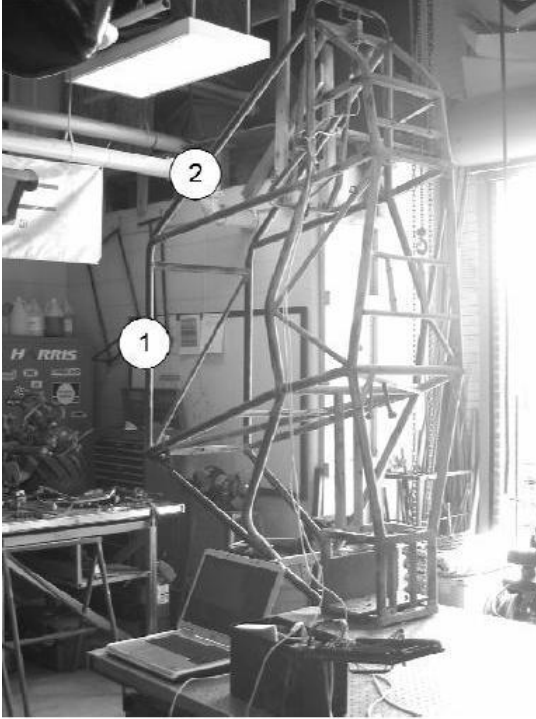
Mode	Numerical Frequency (Hz)	Experimental Frequency (Hz)	Difference
1	23.3	22.2	4.7 %
2	69.9	64.8	7.3 %
3	75.9	71.0	6.5 %
4	88.3	88.6	0.4 %

(a)   (b)
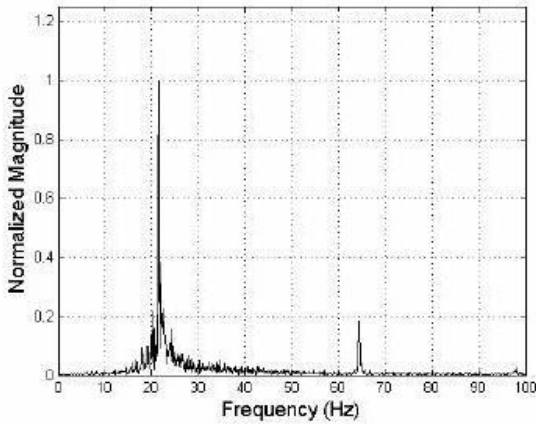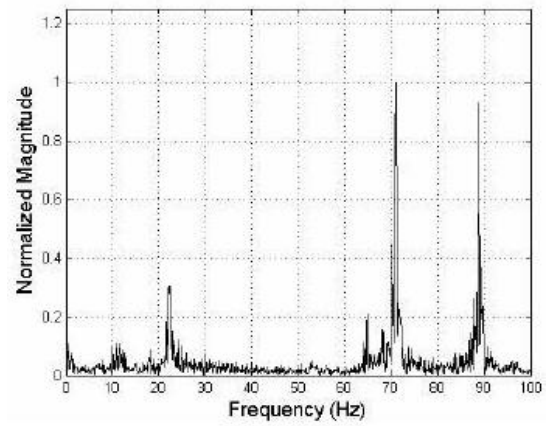
(c)   (d)

Figure 3.4: Modal testing, experiment (a), comparison table (b), FFT of position 1 (c), FFT of position 2 (d) - Source: [13].

14
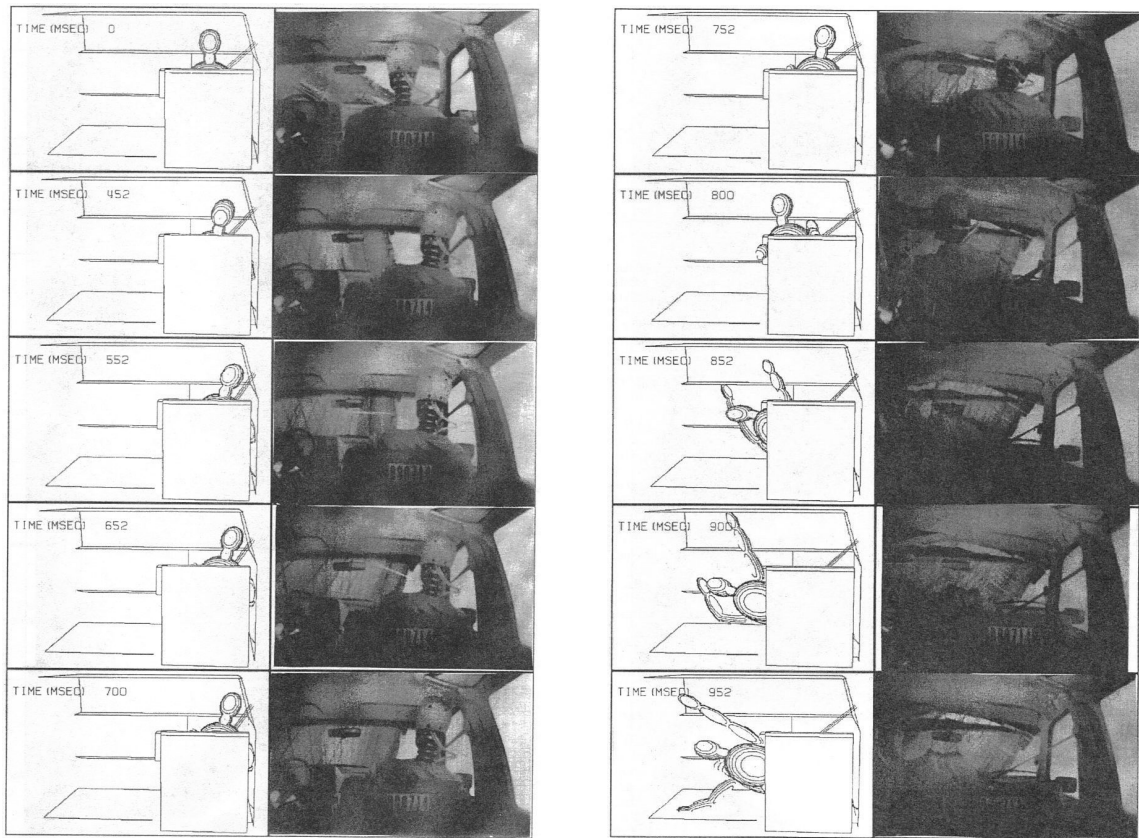
Figure 3.5: Rollover image history, ATB vs. Experiment 1988 minivan - Source: [18]

The second rollover test was called a validation test, and this rollover was simulated with data collected from a rollover of a 1989 Dodge caravan. In this rollover, the minivan completed two full rolls and came to rest on its tires. The video sequence of the rollover and its complement in the ATB simulation are shown in Figure 3.6. When they simulated the rollover in the ATB environment, two components had to be added to make the simulation match well. These components were roof crush and seat belt slack. The roof crush was created in the simulation by hyper-ellipsoid planes that moved into the cockpit in a predefined manner. The seat belt slack was added to the simulation so that the body could move up into position such that it could impact the roof. The results, shown in Figure 3.7, show that the simulation over-predicts the acceleration load. This effect may be due in part to the impact of the dummy with a rigid vehicle. This simulation was described as accurate, however the validity of the simulation was based on knowing the correct values beforehand. There is a limitation to the utility of an ATB analysis where not all the conditions are known.

More work with the ATB program was done by Huanining et al. [5], who simulated a complex vehicle roll over. In this case, they knew the very little information about the accident, but had data on the length of tire marks, total distance traveled after the collision, and number of times that the vehicle rolled. The goal of the work was to create a model that could reasonably re-create the accident. The model of the Toyota pickup in the accident had the exterior modeled as hyper ellipsoid planes and the core of the model was represented as mass and inertia. Although this was a simple model, it was able to represent when the rollover occurred and how it occurred very well. Figure 3.8 shows the drawing of the accident, and the simulated motion of the vehicle. The results of this simulation:

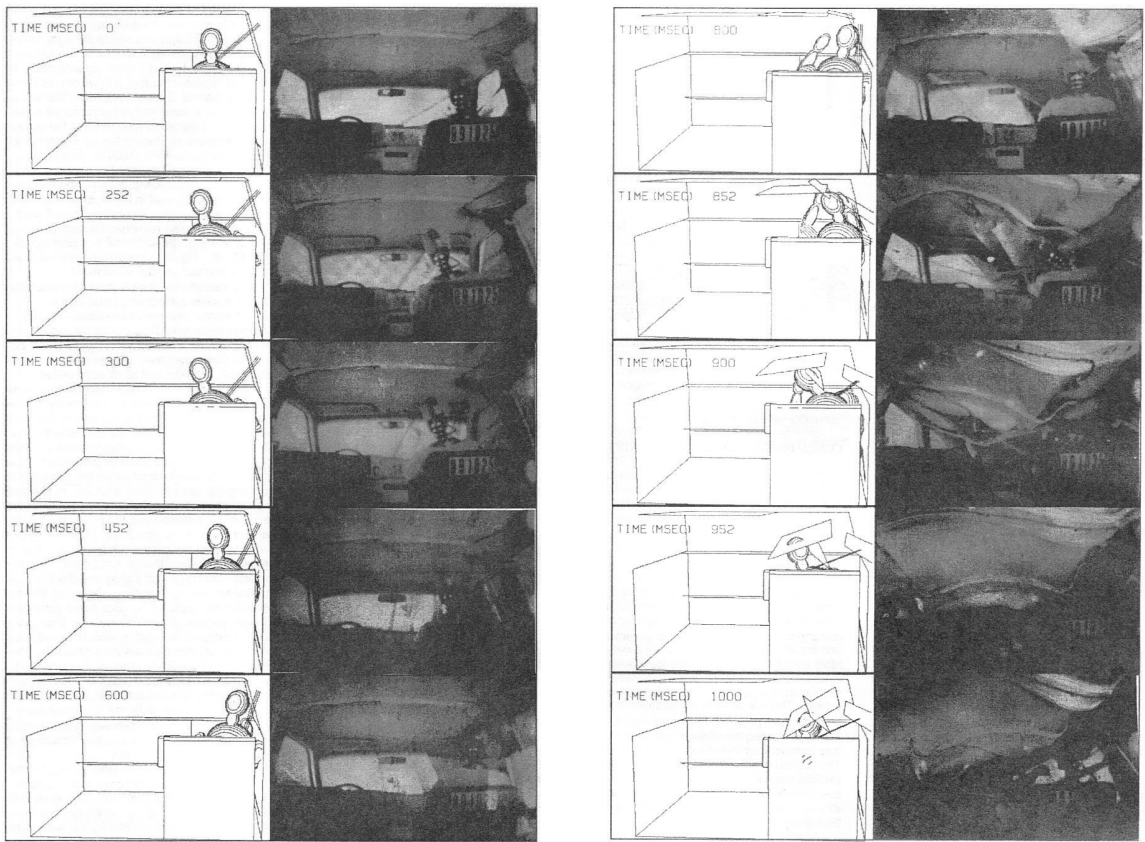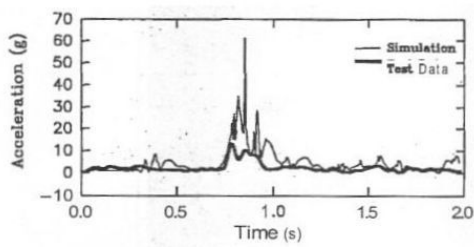Figure 3.6: Rollover image history, ATB vs. Experiment 1989 minivan - Source: [18]

(a)
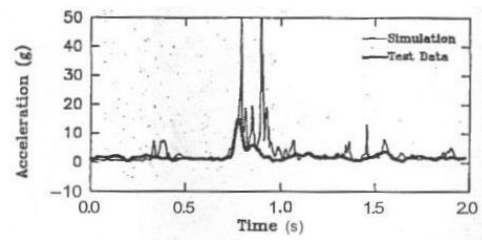
(b)
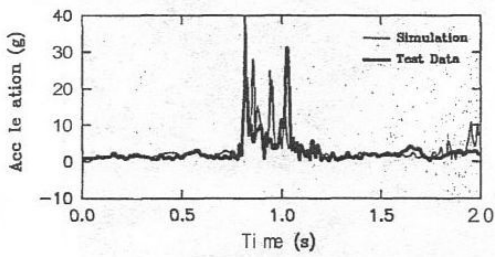
(c)
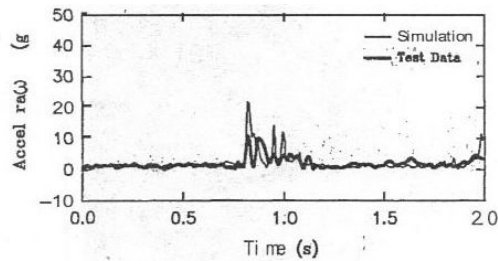
(b)

Figure 3.7: Developmental simulation head accel. (a), chest accel. (c), validation simulation head accel. (b), chest accel. (d) - Source: [18]

18

"In the simulation, the vehicle completed three rolls and stopped 85.1 m from the collision point. The Figure 1 (Figure omitted) measurement is 84.7 m for this distance. Stating from the same yaw angle measured from Figure 1, at the collision point, the simulated vehicle stopped at a yaw angle of -159. degrees, very close to the actual vehicle's orientation angle of -146. degrees in Figure 1. Furthermore, the maximum deflection of the roof created by the roof/ground contact, which is one of the most important numbers, is 0.15 m according to the simulation results. This value is very close to the NASS (National Accident Sampling System) value of 0.16 m, according to the Interior Vehicle Form as illustrated in Figure 2. The simulation also generated a very similar skidding motion in the first part of the accident. The trajectory of this skidding is nearly identical to that shown in the accident diagram, with a simulated forward skidding distance of 15.54 m compared to the actual measured value of 14.33 m in the NASS report [5]."

Huanining et al. continued their work in the same accident, applying the data from the simulated rollover to occupant response [6]. The roll-over of the Toyota truck resulted in a passenger being ejected out the window, and their goal was to show that the simulated occupant was also ejected out of the vehicle. The data for the vehicle rollover was obtained in [5], and was subsequently used in this model. Instead of the vehicle being shown as an external assembly of hyper-ellipsoid planes, it is now a vehicle interior. The driver and passenger were run separately, but in a specific fashion. Since the contact between the passenger and driver could affect the passenger's body motion, the driver was represented in the passenger simulation as an extra set of contact planes. The motion of the driver is
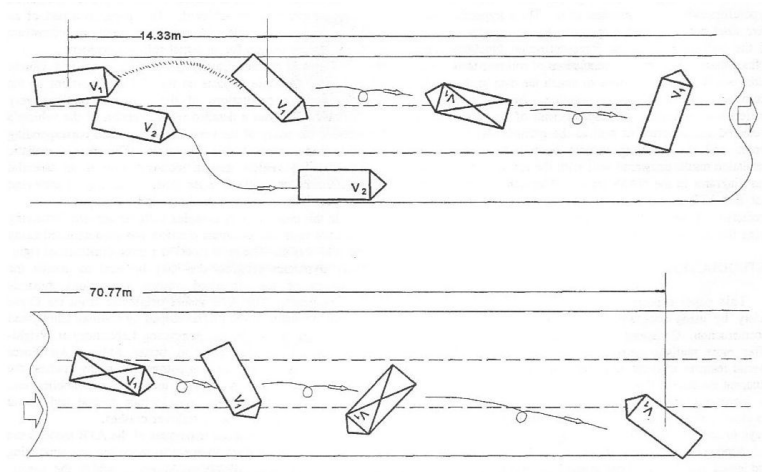
(a)

(b)

Figure 3.8: Witness reports of accident (a), simulation results (b).

shown in Figure, 3.9 (a) and the motion of the passenger is shown in Figure, 3.9 (b). Few results for the passenger are given, but more are given for the driver. The driver, being harnessed by a seatbelt, was injured with cuts and bruises and as such the simulation did not show magnitudes so high as to cause greater injury.

(a)   (b)
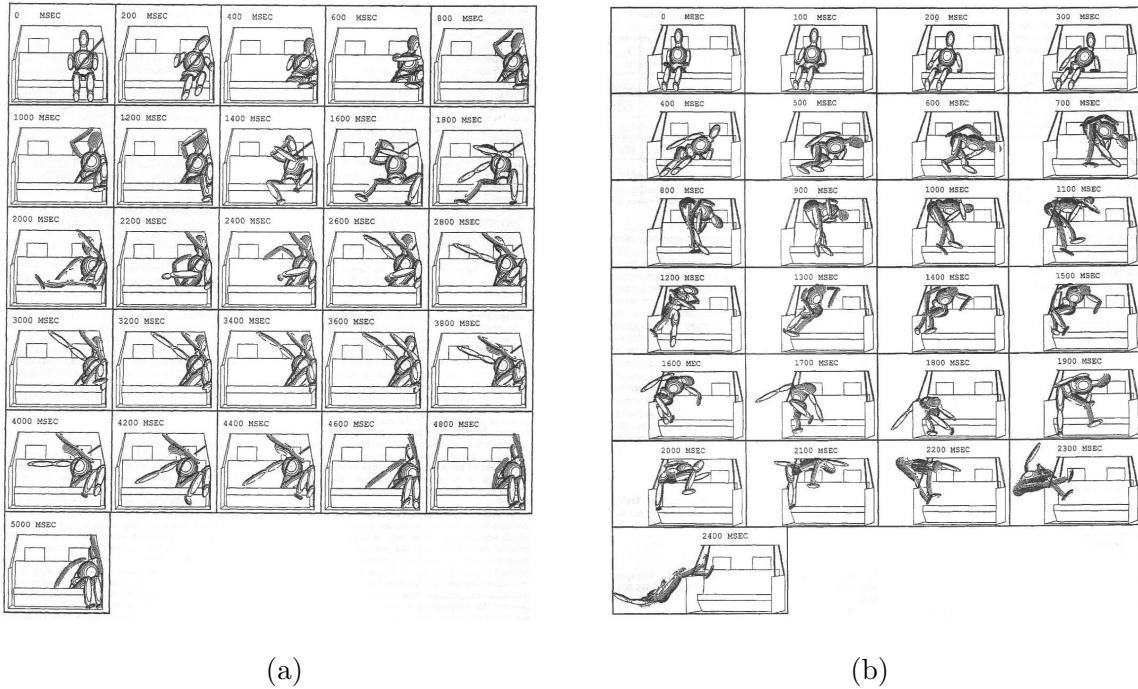
Figure 3.9: Sequence images of rollover in experiment and simulation.

One of the few documented simulations with MSC.Dytran and the ATB program is covered by Fasanella et al. [1], who summarized the results of dynamic work with a crash worthy aircraft body. This simulation was run in the MSC.Dytran/ATB environment so that the interaction of an aircraft structure, seats, and human models could be analyzed. An experimental drop test was done on a prototype composite fuselage with a crushable bottom structure, Jungle Aviation And Radio Service (JAARS) energy absorbing seats,
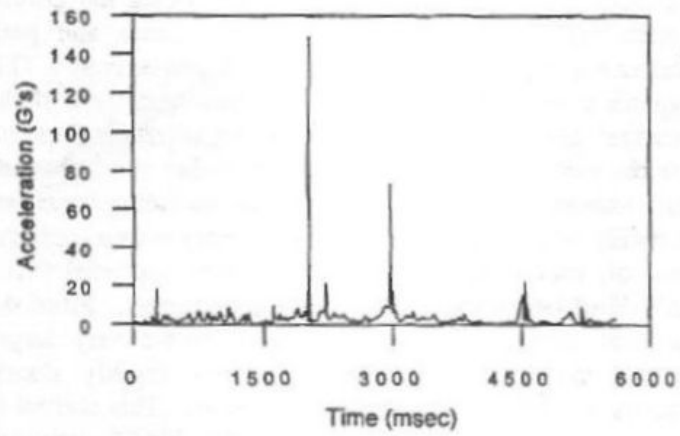
Figure 3.10: Passenger head acceleration results - Source: [6]
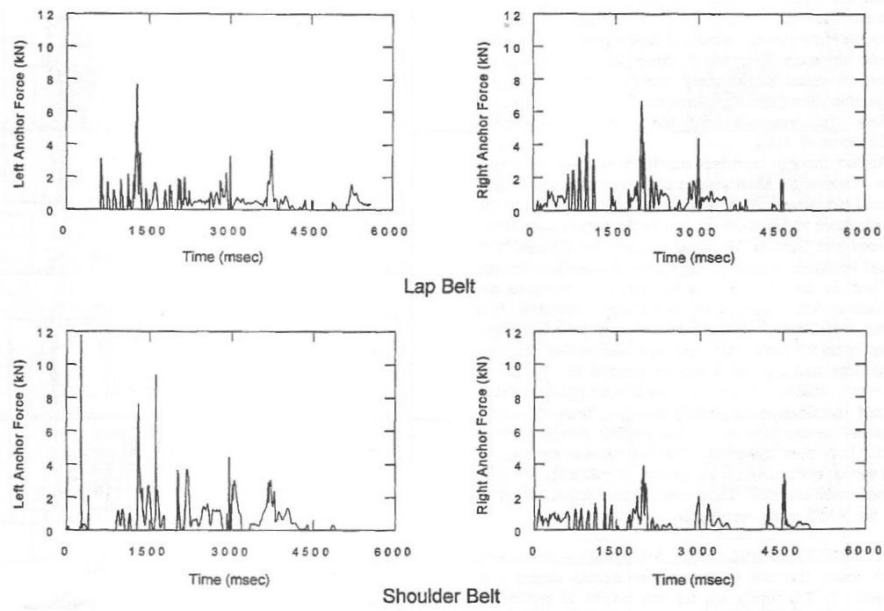
Figure 3.11: Driver seatbelt load history - Source: [6]

and 50th percentile Hybrid II dummies. The experiment is shown in Figure 3.12 and the MSC.Dytran model is shown in Figure 3.13.
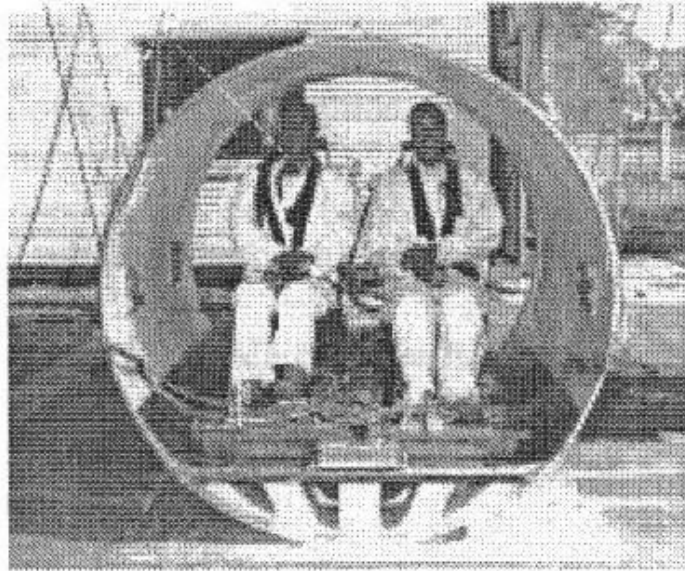
Figure 3.12: Experiment drop test - Source: [1]

This model included many non-linear effects, including plastic deformation of the sub-floor's crushable foam, the seat frame and seat cushion's ability to absorb energy. The results compare the acceleration histories from accelerometers mounted on the floor of the substructure as well as pelvic accelerations from the dummy. The results find that there is good agreement with the magnitude and duration of the acceleration pulses.

The previous work done shows the limitations of the using the ATB program alone and the advantage of using it in combination with MSC.Dytran. A kinematic solver like the ATB program cannot solve for finite element stresses and geometric changes, and a

(a) Front view – full model

(b) One-half cut of the model

(c) Seat frame model, 3-D beam visualization
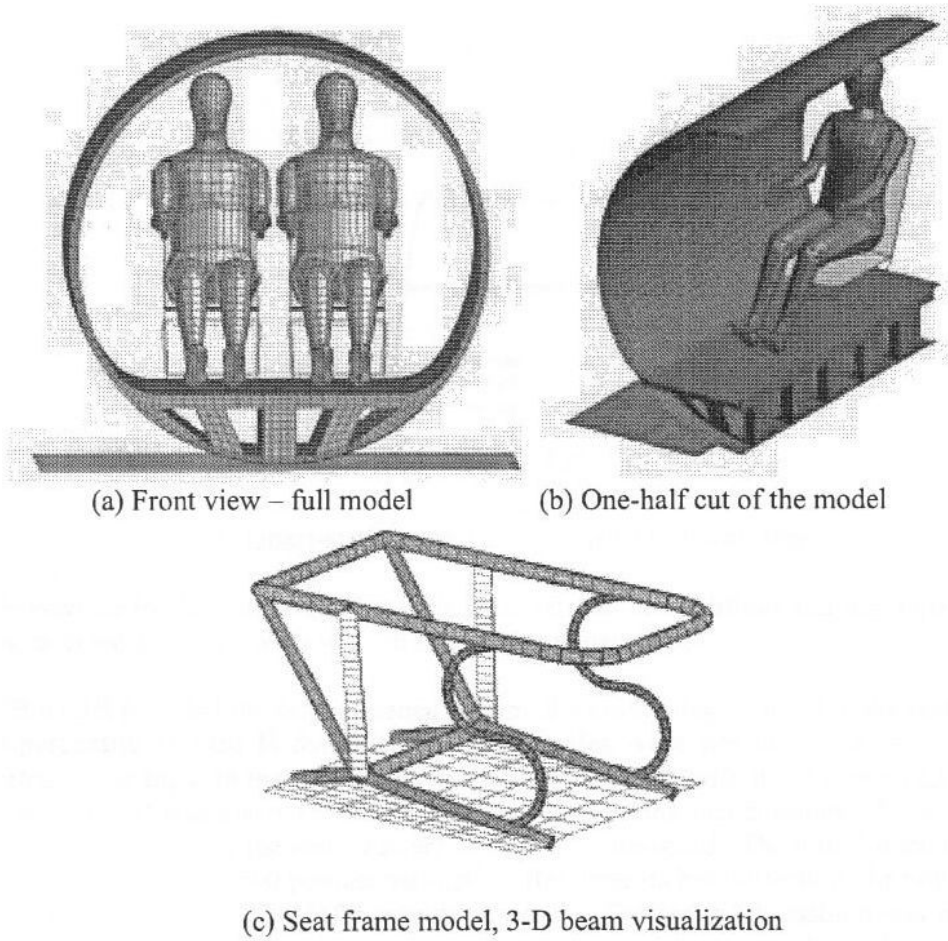
Figure 3.13: FEM illustrations - Source: [1]
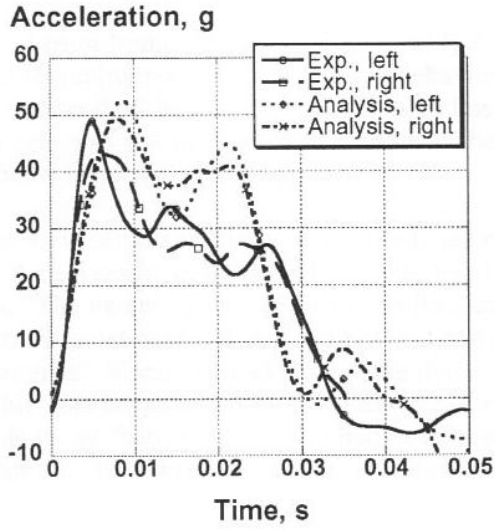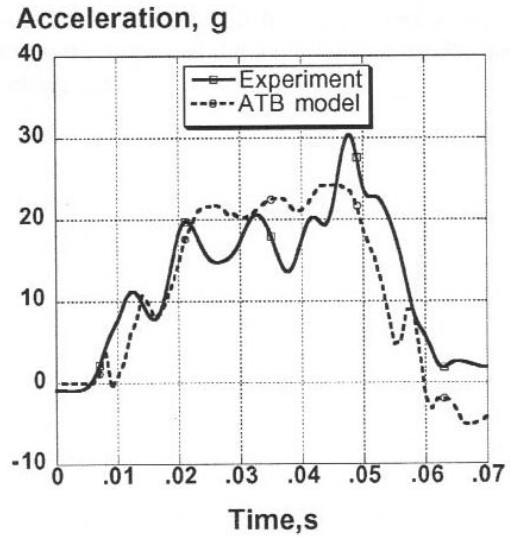
Figure 3.14: Fuselage accelerometer results (a), Hybrid II dummy results (b) - Source: [1]

non-linear transient solver like MSC.Dytran cannot solve for occupant kinematics. The two programs running concurrently allow for occupant and structure interaction, which is important when the dynamic response of the occupant has a significant effect on the response of the vehicle system. The design of the Baja SAE vehicle allows for the entire structure to be analyzed with high fidelity. With the entire Baja SAE vehicle in the simulation, the response of the occupant can drive design changes in the entire vehicle, not just a subsection as was done in [1]. The development of this simulation was unique in that the entire vehicle was modeled.

CHAPTER 4

DEVELOPMENT OF AN OCCUPANT AND VEHICLE INTERACTION SIMULATION

The goal of the occupant and vehicle interaction simulation was to develop a computer model where a simulated occupant would interact with a simulated vehicle, through the seat and seat belts. A force or combination of forces can be applied to the vehicle, and the vehicle can interact with the occupant. By applying the load to the vehicle, the occupant and vehicle interaction model can simulate a much wider variety of load cases, especially those where the inertia of the system as a whole is important. The final model developed has approximately 11,000 degrees of freedom.

The occupant and vehicle interaction simulation uses both the MSC.Dytran and the ATB programs running concurrently. Each of the programs requires their own input file; an .AIN file is for use in the ATB program, and a .DAT file is read into the MSC.Dytran solver. Each of the programs were developed to run independently and so there are many redundant inputs between the two. The .DAT file contains the input data for MSC.Dytran, including the control statements for the simulation, output requests, the finite element model, and parameters for contact. The .AIN file contains the input data for the ATB program, and contains information about the occupant model. Since the ATB program is an independent program, it requires position data for the occupant in the file. The example files included with the release of MSC.Dytran [12] had the characteristics that the ATB input file provided: the seat, occupant mass and joint properties, and the contact functions between the seat and body; while the MSC.Dytran input provided the human body position, seatbelt

mesh, seatbelt properties, and the interface between the MSC.Dytran and ATB programs. This was not adequate since a finite element seat, developed in MSC.Dytran, was required.

4.1   Construction of a Finite Element vehicle

The simulated vehicle was comprised of four parts: the frame, seat, seat belts, and point masses. The frame is a mesh of beam elements with approximately 4674 degrees of freedom. It has adequate fidelity for the seat, seat belts, and point masses to all integrate with it. To integrate the occupant model into the vehicle, it was essential that the vehicle be in the occupant coordinate system, which was with the positive Z direction point into the ground [7]. The seat is a mesh of quadrilateral shell elements that support bending. It has two components, the firewall and the seat bottom, that for the purposes of the simulation are tied together. The complexity of the seat bottom was too high to be practical to model. The seat component has approximately 5448 degrees of freedom. The element mesh density of the seat is higher than that of the mesh on the dummy. This is important because the slave surfaces, which in this case are the seat surfaces, must be finer than that of the master surface, which in this case is the occupant model, as noted in the MSC.Dytran users guide [12]. The seat connects to the frame through 59 grid points. For the firewall part of the seat, these grid points are positioned in approximately the same location of the clamps that mount the experimental firewall to the frame. For the seat bottom, a surface was created on the seat mounting structure to represent the bottom of the seat, and for the seat back a surface was created from the bottom of the seat up to the firewall, as shown in Figure, 6.9. The seat belts connect to the frame in the same locations as the experimental belts. The shoulder belts loop around a tube and back onto themselves to provide an attachment.

This effect was not practical to reproduce, so the simulated belts connect directly to this tube. The belts are rod elements that support a special MSC.Dytran specific belt routine, and they represent 1500 degrees of freedom. All the belt nodes are used as slave surfaces in contacting the occupant model's master surfaces. The point masses represent components of the vehicle whose mass has an effect on the simulation, but whose stiffness does not have a large influence on the results. The point masses represent the suspension, engine, and transmission of the vehicle. These points represent a mass of 141.45 kg (311.84 lbs), and are positioned in the approximate positions of the centers of gravity of the corresponding experimental parts. The total mass of the vehicle without occupant was 174.63 kg (384.99 lb).

4.2 Tuning the properties of the vehicle

The mass of the simulated vehicle needed to match the experimental vehicle for the validation. Getting the mass correct was important so that the same applied force between both the simulation and experiment, produces the same gross accelerations. Tuning the mass of the vehicle was a two step process. The first step involved only the Baja SAE vehicle's frame. Since the frame was the component used to determine modal frequency response, its mass had to match between the simulation and experiment. The finite element frame was built with sufficient detail to provide all major mounting points for the point masses referred to in the previous section. To match the mass of the simulated frame to the experimental one, the density was adjusted to 8846.23 kg/m^3 (0.68086 lbs/in^3). This resulted in a final frame weight of 34.33 kg (75.69 lbs), which matched the mass of the experimental frame. The moment of inertia and the center of gravity of the vehicle were

not adjusted. The dynamic validation constrains the motion of the vehicle in the Y and Z directions, only allowing it to move in the X direction, so the position of the center of gravity will not affect the acceleration in the X direction. Note that the constraints in the Y direction were applied at the suspension interface points, and in the Z direction they were applied at the shock absorber interface points.

The simulated occupant mass had to match the experimental occupant as well. A 95th percentile Hybrid III dummy was used to represent the occupant in the simulation. A 95th percentile occupant has a body height and weight for a person that is statistically within the top 5 percent of the tallest person in the study group. In this case this group was 2420 male subjects in an Air Force research study [14]. In this study, the height of a 100th percentile subject would be 1.96 m (77.0 in), which is the height of the experimental occupant. As such, the simulated dummy should be shorter by about 5% or 0.01905 m (0.75 in). The height was able to be adjusted, however this is not a trivial matter and was out of the scope of this validation. The mass of the simulated occupant needed to be adjusted, and it was assumed that for a change in weight of 13.60 kg (30.00 lb), all the appendages of the body would change by the same percentage. For large changes in body size, it is assumed that the appendages of the body may change at different rates. The final mass of the occupant was 113.40 kg (250.0 lbs). This produced a total system mass of 292.57 kg (645.00 lbs). The simulated occupant did not exactly match the position of the experimental occupant. The simulated dummy did not have their forearms resting on their upper legs, and there was no constraint of the hands like the experimental occupant had with the steering wheel. The differences betwen the two are shown in the results section

under gross body motion.

Contact routines were used in this model to apply similar loads to the occupant between the simulation and the experiment. These contact routines allow the occupant to move in all degrees of freedom. The occupant's motion is restricted only by the interaction between the seat and the seat belts, which are similar to the conditions of the experiment. The simulation solves the first .0001 seconds without contact routines in order to allow the integration routine to stabilize. Since the body is well restrained inside the vehicle, contact is limited to specific areas. The contact of the head of the occupant with the seat is an example of a contact that will occur in a specific area. Reducing the size of the contact areas reduced the total number of contacts that had to be computed, which lead to a drastic decrease in computation time. The initial conditions for contact are different between the ATB program and the MSC.Dytran program. In the ATB manual [7], it is suggested that the body be initially positioned so as to penetrate the seat an adequate amount to balance the forces and come close to making the occupant static. This initial position is based on the balance of the contact planes with the occupant, and is possible due to the formulation of the contact routines in the ATB program. In MSC.Dytran the contacts will fail and the occupant will fall through the seat if the occupant has penetrated the contact surface initially. In this way the occupant model must be allowed to fall into a static position. Many parameters were required to correctly model the contact in this fashion. Due to the complexity of the contact input, an example input from this simulation is provided in Appendix 1. Specific values on the contact input had a major effect on the solution outcome. These values include the friction coefficients, and node penetration distance.

The friction coefficients were assumed since there was no data to support their values. The experimental results include several cases where the friction was significant and unknown. However a specific experimental case was run in order to approximate a low friction condition that could be matched in the simulation. The equation used to simulate friction in MSC.Dytran is shown in equation, 4.1 and is from the MSC.Dytran quick reference guide [12].

$$\mu = \mu_k + (\mu_s - \mu_k)\, e^{-\beta\nu} \tag{4.1}$$

In Equation 4.1, μ represents the friction in the simulation, μ_s is the static coefficient of friction, μ_k is the kinetic coefficient of friction, β is the exponential decay coefficient, and ν is the relative sliding velocity. Determining the effects of each of these variables was outside the scope of this research, especially since the experimental friction values were not known. The friction values used in developing this model assume that the static and kinetic coefficient of friction are the same and the coefficient of exponential decay is one. In the work by Fasanella et al. [3], a friction coefficient of .62 was applied, however in this work the coefficient of friction was .12. This value was decided upon after doing a series of cases where the coefficient of friction was modified for the seat belts. The results, in Appendix 2, show that when the coefficient of friction was increased from .20 to .50, the seat belts locked themselves at a artificially high force. In the low friction case, the simulated coefficient of friction was zero. When the simulated coefficient of friction is zero, the seat belt routine has difficultly converging, which lead to high frequency noise as shown in the low friction results section.

The penetration check and penetration distance inputs were essential to obtaining a well behaved solution. In an early case, the acceleration history of the head and chest had numerous asymptotic spikes of acceleration that could not be explained, and made the data unreadable. One explanation for this was a lack of fidelity in the seat, and that more elements were needed to match the nodes between the seat and the body. However, the spikes in the data were reduced from hundreds to one or two by allowing the body to penetrate the seat and remove some of the grid points from the contact solution. The penetration check provides a method to deactivate some of the slave nodes of the body when they have penetrated a set distance, which is the penetration distance value, through the contact surface. By making this change, grid points that penetrated too far, and thus would have had the most reaction force on them, were eliminated. It is assumed that these handfuls of points with high normal forces, would have had equally high frictional forces, and due to the points moving across the elements in the contact there were discontinuities in the results. Thus it is assumed that the effect of distributing the contact forces evenly among many grid points greatly reduces the amount of acceleration spikes.

Building the finite element model for the vehicle in this simulation was not a trivial matter. There were numerous specific data inputs that were essential to getting well behaved contact routines. The final model uses a completely flexible finite element structure interfacing with the rigid shells of the occupant. In validating the performance of this model, a series of tests had to be developed which could be applied to both the simulation and the experiment.

CHAPTER 5

VALIDATION

To validate that the simulation produced accurate and reproducible results, two validations were done, a modal validation and a dynamic validation. A static validation for the vehicle was determined to be time prohibitive since the validation required significant construction of test apparatus and validation work had already been done by Owens et al. with adequate results [13]. The modal validation used the finite element solver MSC.Nastran and consisted of determining the natural frequencies for the vehicle under specific set of circumstances, and then determining how well the simulation matched the experiment. Due to the complexities of the entire vehicle and possible non-linear effects from the tires and suspension system, only the frame of the vehicle was chosen to do the modal validation. The Baja SAE vehicle frame interconnects all components of the vehicle and provides a load path for applied forces, making it an ideal component to study. The modal response of the vehicle frame must agree with results from the simulated frame in order for the dynamic response to be in agreement. The dynamic validation, which was done in the MSC.Dytran environment, compared the simulated vehicle and occupant versus the experimental vehicle and occupant in terms of the seatbelt loads, accelerometer output, and gross occupant motion. This validation took into account the vehicle as a complete system, including point masses for the tires and suspension components as well as the engine and drive-train. The effect of certain variables like friction coefficients and pretension in the seat belts on the simulation had to be determined through running several different cases. In order to determine these effects, cases with low contact friction, low belt pretension, and high belt pretension were

run. With the modal response of the frame, and time history output from seat belt loads and occupant accelerations, the performance of this model was validated.

5.1   Modal Validation

A modal validation of the finite element model seeks to prove that a finite element model depicts a real structure by comparing natural frequencies and mode shapes. In the work by Silva et al. [16] a random vibratory load was input by shaking equipment into their frame so that they could determine the frequency response function of the frame via accelerometers. Since shaking and high-bandwidth data acquisition equipment were cost prohibitive, the method chosen to determine frequency response was to input a near instantaneous force into the frame and record the acceleration output from a single point on the frame as it resonated. Moving the accelerometer to different points on the frame allowed for the determination of natural frequencies with respect to specific mode shapes. In order to accurately compare natural frequencies between the two models, similar boundary conditions had to be applied in the form of constraints.

5.1.1   Constrained Modal Solution

A constrained modal solution was run since it was not possible to replicate a true free-free boundary condition in which the vehicle has no interaction with external structures. An overall example of the modal validation system is shown in Figure 5.1. In other modal validations, it is common to suspend the structure in question by a bungee or similar restraint to replicate the free-free condition [16]. This has the effect of creating a system by which the structure that is being analyzed has much higher stiffness than the suspension

mechanism, and so the frequency output is dominated by the response of the structure. Since it was unknown how a suspension mechanism would interact with the experimental structure, this method was discarded. The specific concern was the possible interaction of rigid body motion with natural frequencies due to the impulse load. The method chosen was to constrain the experimental structure with rigid boundary conditions, which can be replicated in the model. A detail of the experimental structural constraint is shown in Figure 5.2.

A rigid boundary condition is not actually possible to replicate due to finite modulus of elasticity and inertia in the constraining structure. It is assumed that the stiffness of the constraining structure is much higher than that of the experimental structure, and so the frequency response of the experiment is not influenced by the response of the constraints. In order to apply these constraints in the simulation, single point constraints were utilized, which apply an enforced displacement to the model. In a constrained case, the displacement is zero and has the affect of removing rows and columns of specific degrees of freedom out of the stiffness and mass matrices. As will be seen in the results chapter, the frequencies of the first three modal solutions in the simulation had significant error. In order to determine if the error could potentially be from incorrect assumptions about the boundary conditions, another model was developed with different boundary conditions. This model added a part of the constraint structure, the table top, to the model. This table top was a rectangular mesh of quadrilateral elements that supported shear and bending loads. A thickness for the tabletop, which determines the cross-sectional moment of inertia, was assumed since this value was unable to be determined experimentally. The tabletop structure was supported by a steel framework that was assumed to be very stiff in comparison to the tabletop and

the frame. The supporting steel framework was modeled as pinned nodes at the table top interface points. The results of this solution are shown in Appendix 1, and suggest that the stiffness of the tabletop could potentially be low enough to interact with the first three modes of the experimental structure. This potential effect cannot be made certain without more experimental modal solutions using a variety of boundary conditions.

5.1.2 Determining Natural Frequencies

The natural frequencies of the experimental structure and the simulated structure had to be determined in order to compare them. To determine the natural frequencies of the experimental structure, the Baja SAE frame was excited by an impulse load and this excitation was recorded by accelerometers. The natural frequencies of the vehicle frame were also determined using the eigenvalue solver in MSC.Nastran.

The natural frequencies of the experimental structure were found by applying an impulse load to the frame and allowing it to resonate. The applied load was an impact by the palm of the hand to the frame, which from previous work was known to produce cleaner response than impacting the frame with a hammer or mallet. Reproducing the same magnitude of the force applied to the frame was not essential since the frequency response was used. It was not possible to obtain accelerometer data from many points along the frame simultaneously, otherwise the magnitude of the applied force would have to have been known in order to get the frequency response function. Using the finite element modal solution as a guide, positions were found that represented the location of highest deflection for a particular mode. This allowed for nine positions to be identified. These positions resonate

Figure 5.1: 2005 Baja SAE Frame under modal evaluation

Figure 5.2: Physical constraints for the modal evaluation

at higher magnitudes for some modes and not others, allowing for frequencies to be matched with mode shapes. The Analog Devices ADL302 accelerometer can detect frequencies up to 100 hz before the on-board capacitors begin to low pass filter the data. Frequencies up to 112 hz are recorded, and through the use of Fast Fourier Transforms (FFT), the response can be separated into frequencies. The FFT solver used in this work was derived from an example program off of the MATHWORKS website [10]. Note that the FFT is a special implementation of the Discrete Fourier Transform or DFT, and accepts a time-varying function as input and computes the frequency spectrum of this signal [2].

The stiffness and mass matrices of a Finite Element model have distinct eigenvalues and eigenvectors. The eigenvalues represent the frequency of a mode, and the eigenvectors represent the shape of the mode. The Lanczos method in MSC.Nastran was used to determine the eigenvalues and eigenvectors. The Lanczos method uses Krylov subspaces to reduce the original matrix to a sequence of matrix problems [19].

The formulation of the mass matrix can have an effect on the results. A lumped mass matrix formulates the matrix such that all the mass along a beam or a shell is placed at the nodes, with no dynamic coupling between the element displacements [15]. This makes the mass matrix diagonal and sparse which makes it faster to compute. However using the lumped mass method also produces results that can be lower in frequency than the actual model. A second way to build the mass matrix is called the coupled mass method. This method builds elements with distributed mass and off-diagonal terms which couple translational and rotational inertia. The coupled mass method can be more accurate than the

lumped mass method [17].

Since adding mass to a system with a constant spring rate will lower the original frequency, adding the accelerometer mounting bracket would lower the frequency of the natural modes. How much this effect changed the solution was an unknown. Thus the lumped mass model was run several times with an additional point mass which represented the accelerometer and bracket. Each time the point mass was moved to a different location in order to analyze the effect that this mass had on the frequency. The accelerometer and bracket had a total mass of 0.61 kg (1.35 lb), and was made of an aluminum center with steel end caps. The mounting block for the accelerometer is detailed in Figure 5.3. Since this bracket was positioned in different places on the experimental frame, it is reasonable to assume that the experimental frequencies may have changed as well.
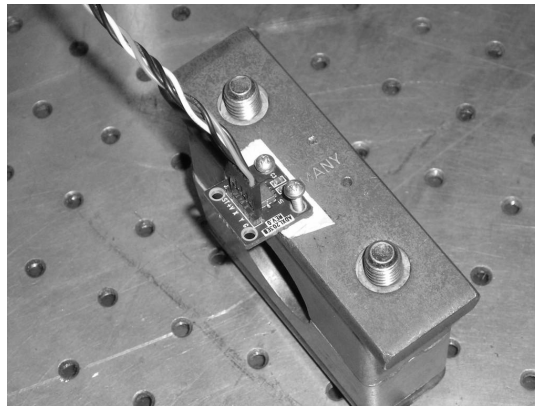
Figure 5.3: Accelerometer and associated mounting bracket

5.1.3 Determining Mode shapes

Specific points on the frame have a much larger response for a given frequency and less response for other frequencies. For instance, the center of the firewall will move in response to an excitation of the first mode which is a pitching motion. However the center of the firewall has no motion when the third mode of the frame is excited. In this way, an accelerometer placed on the center of the firewall should show some response for mode one and very little for mode three. Using the Fast Fourier Transform to translate the accelerometer response data from the time domain to the frequency domain, the frequencies of the body can be found. In addition, the location of the accelerometer and the general magnitude of the response of some frequencies relative to others can indicate which mode shapes are resonating. Using the individual frequencies and their associated magnitudes, an experimental mode and frequency pair can be associated together. This applies to a unique problem in this research whereupon the experimental frequency for the second mode matched the finite element's frequency for the first mode. If experimental frequencies were not matched to specific mode shapes, it would have been incorrectly assumed that the frequencies matched very well, when in fact they are different by approximately 1.5 hz. The first three natural frequencies for the simulated constrained model are 9.36 hertz, 12.62 hertz, and 16.81 hertz. The first three experimental frequencies are 7.97 hertz, 9.85 hertz, and 14.75 hertz. If the original boundary condition is assumed valid, then the first experimental frequency could be viewed as an anomaly, and the other two frequencies valid. However positioning the accelerometer in places of peak response, and analyzing the relative response of some frequencies compared to others validated that 7.97 hertz was indeed the frequency of the first mode of the experimental system.

5.2 Dynamic Model Validation

The dynamic model validation of the occupant and vehicle simulation was done to reproduce the experimental conditions and return similar results. The experimental conditions included the forces applied as well as the belt and seat properties. The experiment was a type of sled test that involved quickly decelerating the vehicle which was moving at a constant speed. For safety reasons, the magnitude of acceleration was kept below 10G's for any part of the body.

5.2.1 Experimental Setup

The experimental vehicle was a 2005 era Baja SAE car, depicted in Figure 5.4. In order to compare the same loads between the simulation and the experiment, three load cells and an accelerometer were placed in specific locations. Two load cells were built into the seat belts to provided restraint data. They were placed on the driver side shoulder belt and the passenger side lap belt as shown in Figure 5.5.

Figure 5.4: 2005 Auburn Baja SAE car

Equipment had to be fabricated to integrate the load cells into the seat belts. It

was critical that none of the load cells receive damaging bending moments, and due to the flexibility in the belt, a large range of motion was needed. Ball and socket joints were used to achieve the desired range of motion. To integrate the shoulder seat belt to the load cell, the belt was redesigned to transition from the fabric of the belt to a ball joint fastener which was fastened to the load cell as shown in Figure, 5.5. On the other side of the load cell, another ball joint was fastened to an adapter which locks into the latching mechanism. To adapt the lower belt, a similar adapter from the belt fabric to the load cell was used, and the frame side of the load cell was fastened to a ball joint which was in turn bolted to tabs, welded to the frame. These parts are detailed in Figure, 5.6.
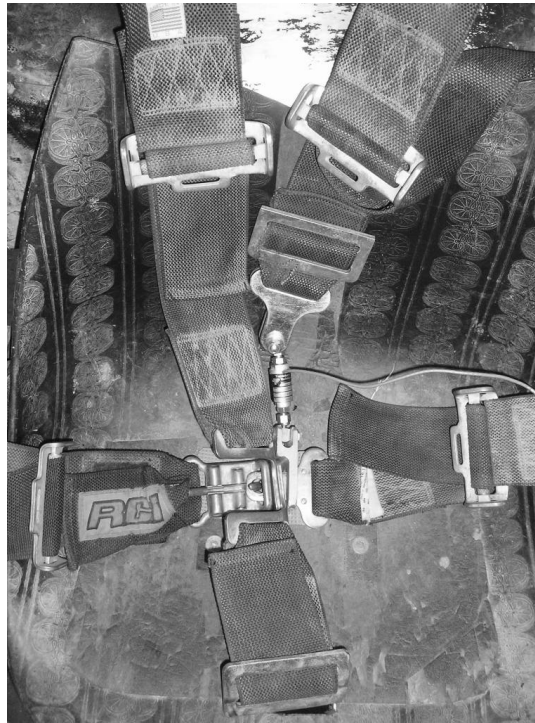
Figure 5.5: Integration of Load cells into Belts

(a)   (b)

Figure 5.6: Detail of Shoulder Load Cell (a), Lap Load Cell (b)

To determine the acceleration history of the vehicle and the occupant, accelerome-
ters were placed at various locations on the system. The occupant had accelerometers
placed in two locations, one on the helmet to resolve head accelerations, and one on the
chest to determine chest accelerations. The ATB program outputs acceleration history for
the body segments in their local coordinate system [7], so the accelerometers for the head
were fixed to the helmet such that they rotated with the head, as can be seen in Figure 5.7
(a). The chest accelerometers were taped to the chest in a loose fashion, as shown in Figure
5.7 (b). However the acceleration of the chest in the simulation is strongly influenced by
the contact routines. There are many unknowns that limit this analysis to the comparison
of rough order of magnitude results and response shape trends.

The applied load to the vehicle had to be known in order to properly load the sim-
ulation in the same way. So that there would be no unknown loads transmitted through
the suspension, the applied load had to be collinear with the center of gravity. In this way,

43
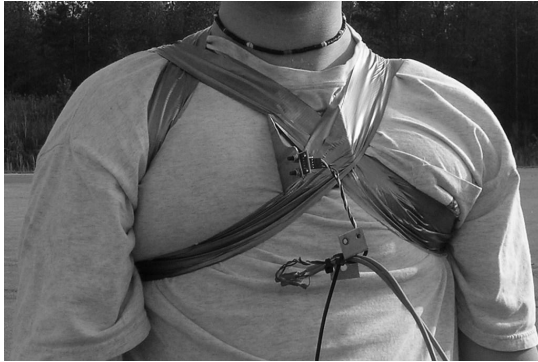
(a)   (b)

Figure 5.7: Helmet Accelerometer (a), and Chest Accelerometer (b).

no moment would be applied to the vehicle, resulting in suspension loads. The center of gravity was found for the combined system of the occupant and vehicle. To find the center of gravity of the system the occupant and vehicle were hung from two points at the top of the vehicle. A plum hung from each of these points would create two intersecting lines. The intersection represents the center of gravity, as shown in Figure 5.8. The engine deck location is an ideal location to load the frame due to its ability to handle structural loads, so no additional structural enhancement was needed. Tabs were used to connect the load cell to the frame, as shown in Figure 5.9.

With the tabs in place, a method was created to load the frame in a repeatable fashion. It was not essential that the pulse be ideal or exactly a sinusoidal curve since an approximation to an analytical model was not the goal. The goal was to apply known loading data and see how the simulation matched the real event. As such, a repeatable method was developed so that seat belt friction would have consistent magnitude. The occupant and
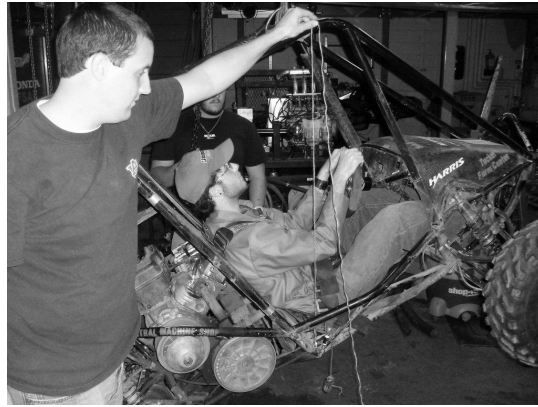
Figure 5.8: Detail of Method used to find Center of Gravity

(a)   (b)

Figure 5.9: Detail of Frame Load cell and attachment

vehicle were loaded by the inertia of the system in motion reacting with the force applied by an elastic strap attached to an immobile structure. A load cell in line with this elastic strap provided the method by which the load history was recorded. This method is detailed in Figure 5.10. The initial testing velocity was similar in magnitude to a persons jogging speed, which produced clean and repeatable data, so no other speed was deemed important to study.

5.2.2 Calibration

The load cells were calibrated for the conditions they were in. These conditions included the supply voltage, attributes of the data acquisition system, and the ambient temperature given the summer season. Since the load cell gave accurate results for a given load range, it was decided to calibrate the load cells in two steps. First every time the load cells were to be used, they would be zeroed for the ambient conditions. Second the load cells were calibrated individually by applying a known load to them and recording the change in output voltage. To give an example, the output of a load cell at rest with the given data acquisition system is shown in Figure 5.1.
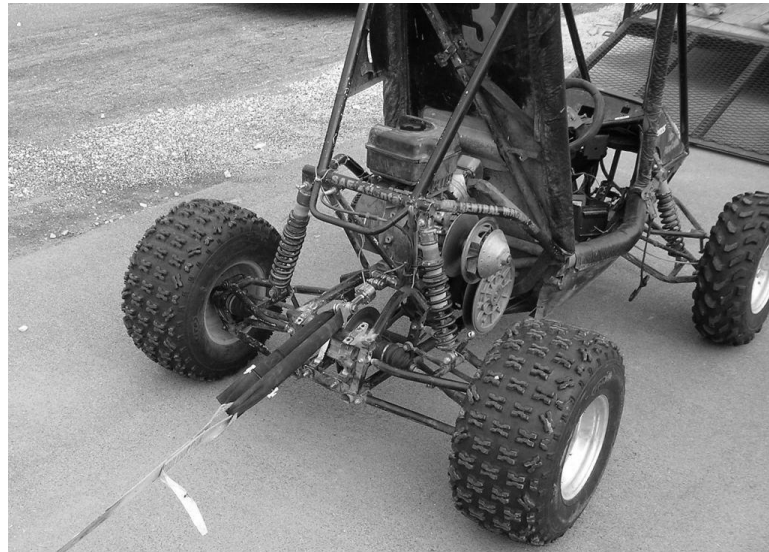
Figure 5.10: Detail of Experimental System

The reason there are multiple bands of values is due to the power supply. The power supply for this acquisition system is a 10 volt regulator, LM 7810, manufactured by National Semiconductor. This power supply is a switching regulator, and thus is assumed to be the
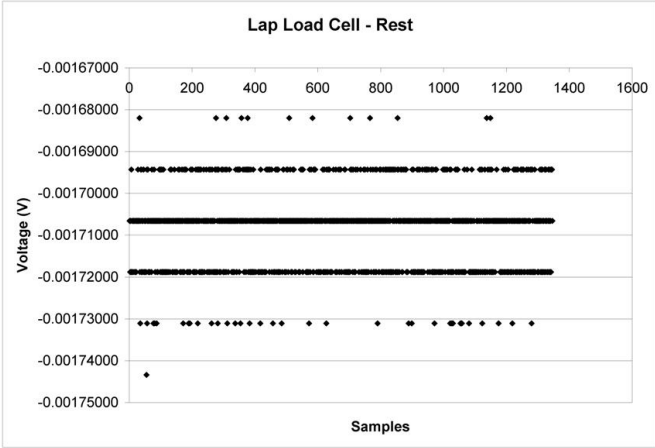
Table 5.1: Plot of Data with Load cell at Rest
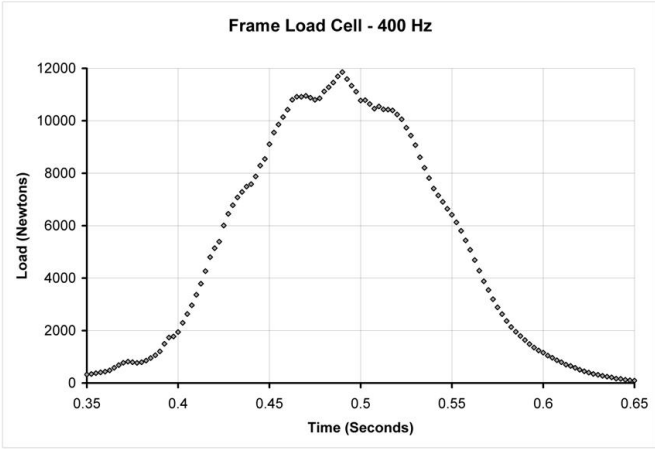
Figure 5.11: Plot of Typical Load vs. Time

47

reason for the different bands of voltages. It is clear that there is a central band of voltage where the majority of the data points are, and this is used as the zero. If such a clear banding was not present, a statical method would have to have been done. A histogram could have been used here to find the value of the zero point [2]. While still connected to the data acquisition device, the load cell is then connected to the testing apparatus. The load cell calibration apparatus is shown in Figure 5.12 and is detailed in Figure 5.13.

Figure 5.12: Calibration Rig

This device allows many different load cells to be tested in tension or compression. The belt load cells were tension only cells. With the known weight of the bar and adding additional weight at known intervals, the force applied at the load cell is easy to compute. An example of the data used to determine the load cell properties is given in Figure 5.14.

In this data, the approximate zero is seen just below the numeric zero. This value

48
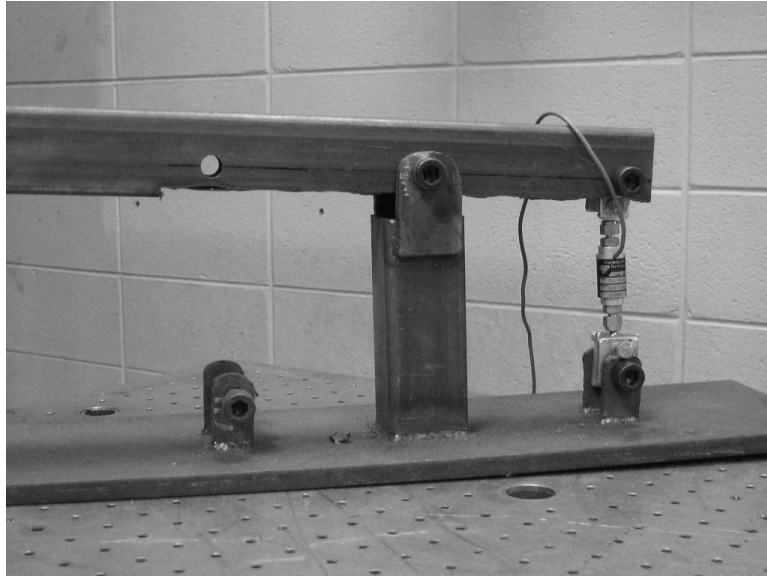
Figure 5.13: Calibration Rig Detail
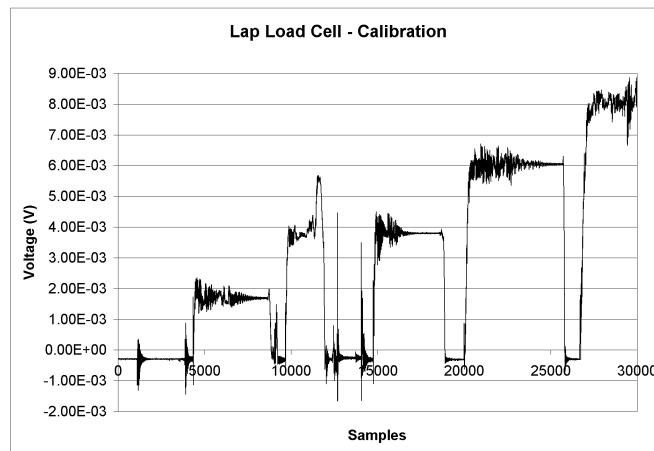
Figure 5.14: Plot of Load cell Voltage

does not drift any sizable amount. There is some excitation of the natural frequency of the bar before it settles on the exact value for the weight. A table was created with the known load and the recorded voltage. The resulting plot of this table is shown in Figure 5.15.
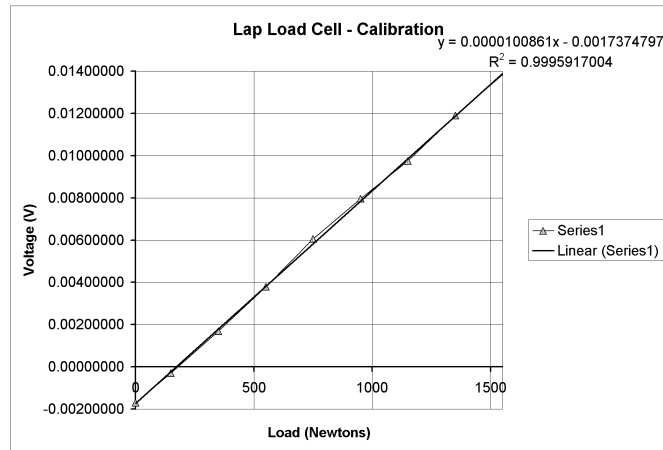
Figure 5.15: Plot of Volts vs. Newtons for Calibration

This result means that the lap load cell was calibrated at 1.00854E-05 Volts per Newton. All subsequent calibrations of the other load cells showed similar linear equations with R squared values above 99%. Using this method to determine the properties of the load cells, accurate load histories could be recorded.

With adequate methods for calibrating the data acquisition system, experiments could be run. However a consistent methodology needed to be adopted to ensure accuracy. This

methodology incorporated the following steps: record baseline values, load body in vehicle, begin recording, accelerate vehicle, decelerate vehicle, and record data.

5.2.3 Belt testing

Figure 5.16: INSTRON - 4500

The properties of the seat belts in the car were determined experimentally for the loading condition. There was no data from the manufacturer on the load versus elongation curve. The seat belts were tested in the Textile Engineering Department at Auburn University on an INSTRON - 4500 machine, shown in Figure 5.16. The belt was attached to the loading rig via hydraulic clamps shown in Figure 5.17. The maximum load applied to the seat belt was 2000.00 N (450.00 lb) and was applied in one second. This load provides a large range of data without increasing the load to a point where the belt will slip in the mounting.

This machine clamped the belt with minimal slippage and produced a table of data of

Figure 5.17: Detail of Belt Mounting
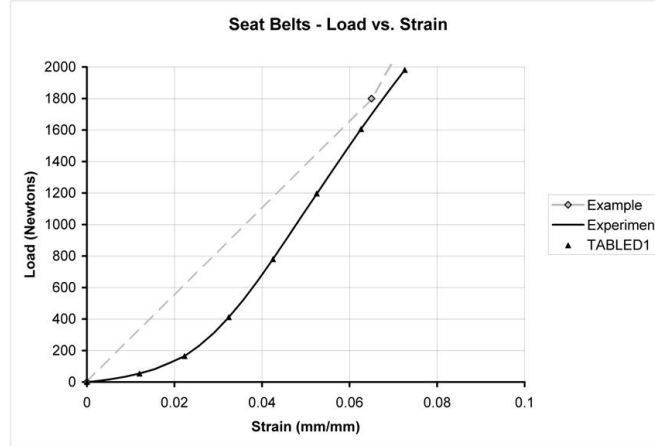
Table 5.2: Plot of Experimental Results of Load vs. Elongation

the load applied versus the elongation. The gage length of the belt was 152.40 mm (6.00 in). The strain rate of the belt was 300.00 mm/min (0.1969 in/sec). It should be noted that after the test was over, the machine held the distance constant. It was noticed that the belt relaxed itself at a rate of .001 Newtons per second, giving an indication of the rate that the belt fibers re-align. The results of the test are shown in Figure 5.2.

This table shows the relationship between the load applied and the strain output. The dashed line represents the values in the example files that came with MSC.Dytran. The solid curve represents the data from the experiment, and the black triangles represent the values input to the simulation in a TABLED1 bulk data entry. The example data continues on to a much higher load, but only has three data points, two of which are present on the table. The new set better represents the loading characteristics of the belt. The

loading and unloading events are acknowledged to be different, however for the magnitude of the forces in this case, they are assumed to be the same.

5.2.4 Cases Run and their Application to the Simulation

Prior to running experiments to obtain data for the simulation, tests had to be run to ensure the fidelity of the data. As such, accelerometer placement was varied as well as sampling frequency to determine that no fidelity was being lost. The sampling frequency was determined to be 2000 Hz, which when divided up amongst 5 channels of input would give a per channel frequency of 400 Hz. This means that each second of data has 400 data points, and since the loading event is 300 milliseconds long, that means that there are 120 data points in each curve. A visual representation of these data points are provided in Figure 5.11.

The belt tension matrix involved three different belt tension levels with three different accelerometer locations. The three belt tension levels were: loose belts, self tight belts, and very tight belts. Although the specific load is detailed below, loose belts were defined as having no tensile load on them, they were free to move somewhat; self tight belts were defined as the highest tensile load the belts could have from the driver's adjustments; and very tight belts were defined as belts that were tightened externally by a person outside of the car. These three cases were run for three cases of accelerometer placement. These three cases were the accelerometer: connected to the frame, the helmet, or the chest. The frame accelerometer was always placed at the top of the roll hoop right in front of the firewall. The helmet accelerometer placement was on a bracket attached to the helmet. The chest

placement was on a plate that was taped to the driver's chest.

The validation work done for the occupant and vehicle simulation is for the load case in which the system is decelerated from the aft of the vehicle in a single direction with no rotations. This load case was simple to experiment and easy to reproduce in a simulation. The flexibility of the solver allows for more complicated load cases, however these cases were out of the scope of this research. These cases might represent matching loads and accelerations for a dynamic motion like a jump, or determining the impact characteristics of the system with a tree. The results of the validation for this load case are shown in the following chapter and provide information on the limitations of the simulation.

The results of the modal validation and the dynamic validation methods in the previous chapter are presented here. The results of these two validations show what parts of the simulation are accurate and the amount of error for parts that are not accurate. It is important to know if and by how much the simulation may over or under predict the solution.

6.1   Modal results

The frame of the Baja SAE vehicle transfers the load due to the applied force to the inertial masses. The simulated model must have a dynamic behavior similar to the experimental model. If the stiffness of the frame is too low or too high, the amount of force transferred to the occupant by the frame may not be correct. The modal analysis compares frequencies and mode shapes of the simulated frame versus the experimental frames to show that the stiffness and mass have been accurately modeled.

6.1.1   Natrual Frequencies of the Experimental Frame

The natural frequencies of the frame were found through applying an impulse load to the frame and then recording the response in different places with an accelerometer. That data was then converted via Fast Fourier Transform from the time domain to the frequency domain, producing peak responses at specific frequencies. In order to know where to place the accelerometers, the finite element modal analysis was done first. The results showed

distinct places were the structural response was highest for each mode. Many of the accelerometer locations will record the response of many frequencies. In other positions the accelerometers will be at a vibration node, and have small displacements for that frequency. The positions of the accelerometers are shown in Figure 6.1 to aid in comparing the positions with the locations of peak deflection in the NASTRAN modal analysis shown later in Figure 6.7.
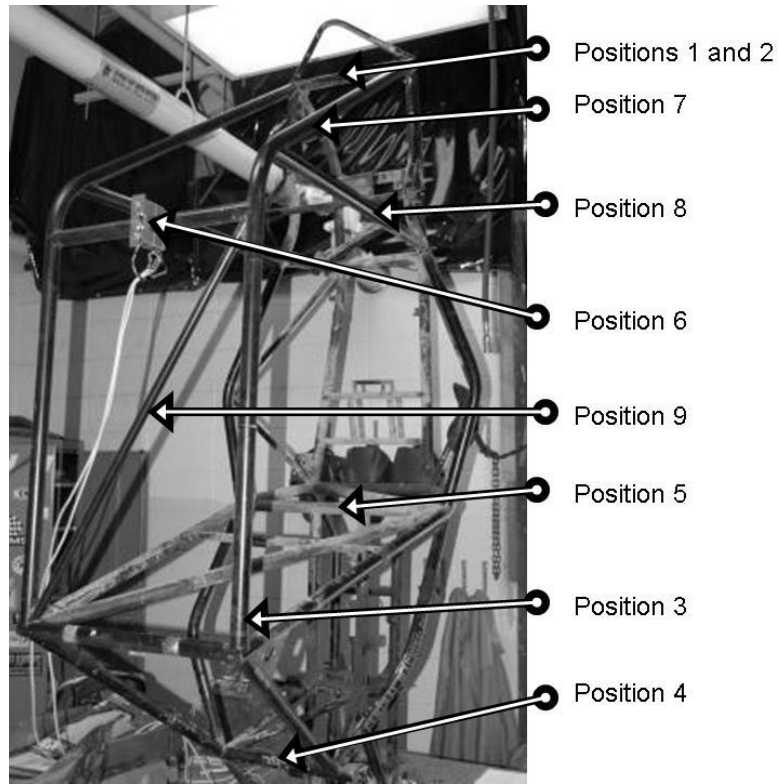
Figure 6.1: Position of the accelerometers in relation to the experiments.

At every position, the frame was struck in a fashion so as to excite the natural frequency associated with that position. An example would be for the first two positions (they are collinear), which exhibit a pitch mode in one direction and a yaw mode in another, both

57

directions would be excited independently. For the first few three frequencies, the motions were able to be seen with the naked eye, but for the higher frequency modes, it was not able to be seen. The Fast Fourier Transforms were computed with a generic MATLAB code [10]. A scaling factor was applied to the set so the frequencies could be better seen.

(a)   (b)
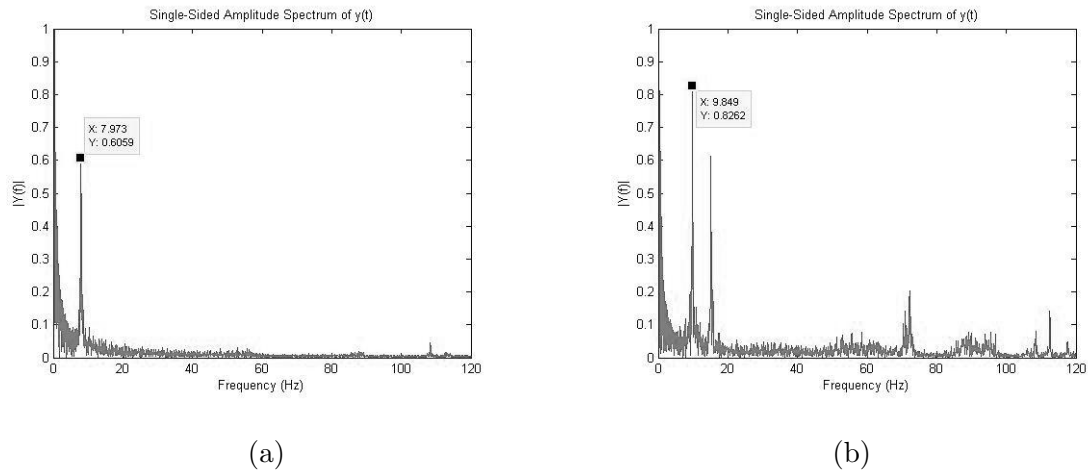
Figure 6.2: FFT of data from position 1 (a), and position 2 (b).

Figure 6.2, shows the FFT of both position one and position two. Position one is a pitch mode, and so with the accelerometer on the nose of the frame, oscillations in the pitch direction have the greatest amplitude. It has a high response at an isolated frequency of 7.97 hz, which is unquestionably the 1st mode. However, referencing the MSC.Nastran results Table 6.4, the results for the 1st mode should be a bit higher than 9 hz. This shows the utility of positioning the accelerometer in a way to isolate a specific frequency. Position two is a yaw mode, and is the accelerometer in position 1 turned ninety degrees in order to isolate the yaw frequency of 9.85 hz. The forces applied in the Y direction excited the second and third modes, and it is clear that the second mode has the highest response.

There is also a response from the sixth mode, at 72.28 hz. For position two, the sixth mode should represent a vibration node of no displacement, however this result would seem to indicate that there is enough lack of symmetry to produce a significant response.
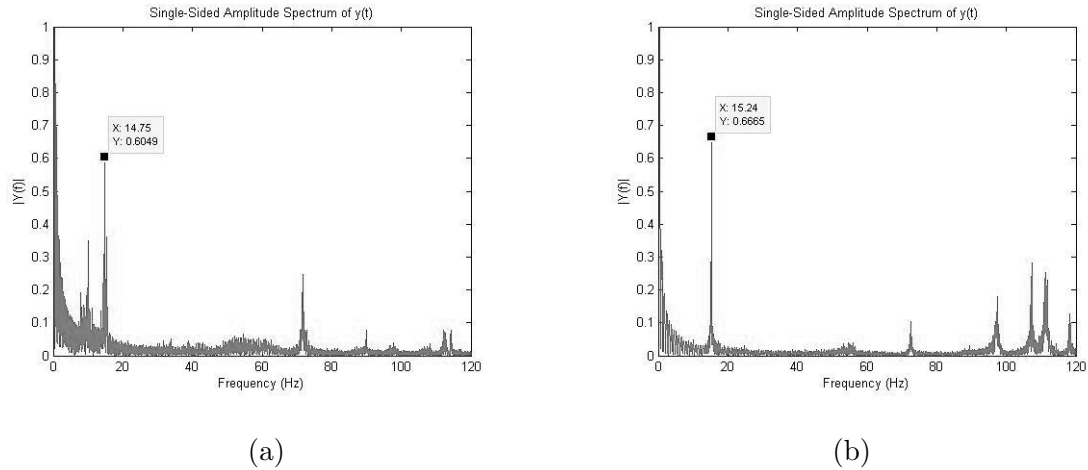
Figure 6.3: FFT of data from position 3 (a), and position 4 (b).

Figure 6.3, shows the FFT of both position three and position four. For position three, the accelerometer was placed at the top of the firewall, near the intersection with the roll halo. The frequency 14.75 Hertz has the highest magnitude, indicating that it is the third mode. At this accelerometer position, the second and sixth modes show high response. Position four located the accelerometer at the center of the rear shock tube in order to get the fourth mode's rocking motion as shown in Figure 6.7. The response is dominated by the third mode, and the response of the fourth mode is barely present with almost no response at 54.95 hz. The sixth mode is also present.

Figure 6.4, shows the FFT of both position five and position six. The placement of
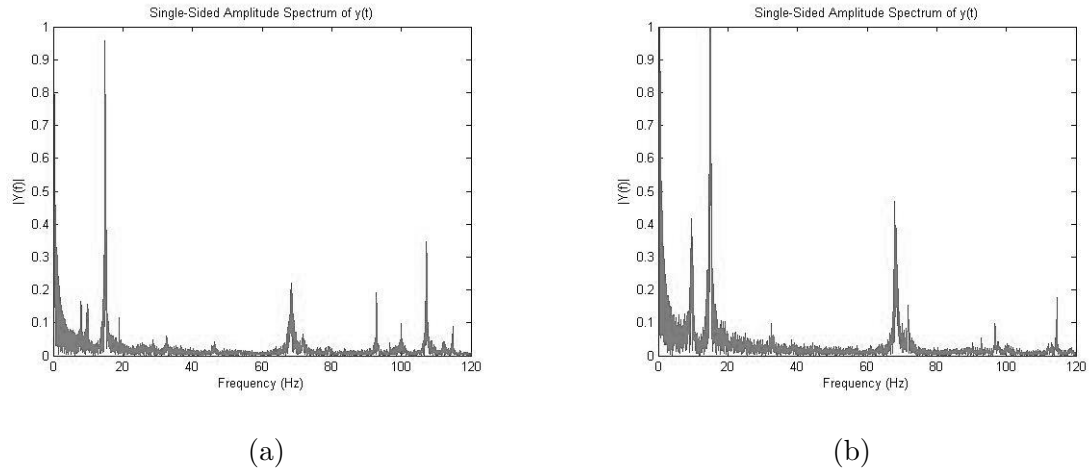
Figure 6.4: FFT of data from position 5 (a), and position 6 (b).

the accelerometer at position five was at the firewall mid-plane; this position should have high response to mode five and low response to six. The results show that mode five, at 68.34 hz, is indeed resonated, however not to the degree expected, mode three dominates the motion. Although mode six should not have been present, a very small response for six is shown at 71.85 hz. Mode three should specifically be absent, but it has the highest response. It is proposed that the impact that drives the modal response of the system deflects it enough that vibrational nodes are moved to a degree that those frequencies show up on the accelerometer. Also mode three has a very strong vibration that can be seen with the naked eye, so it can overpower other modes. The accelerometer at position six was placed on the front halo tube specifically to be excited in the side to side direction. The results of the FFT show that mode six, which has shown up consistently in earlier results, barely shows up as a peak on the side of mode five.
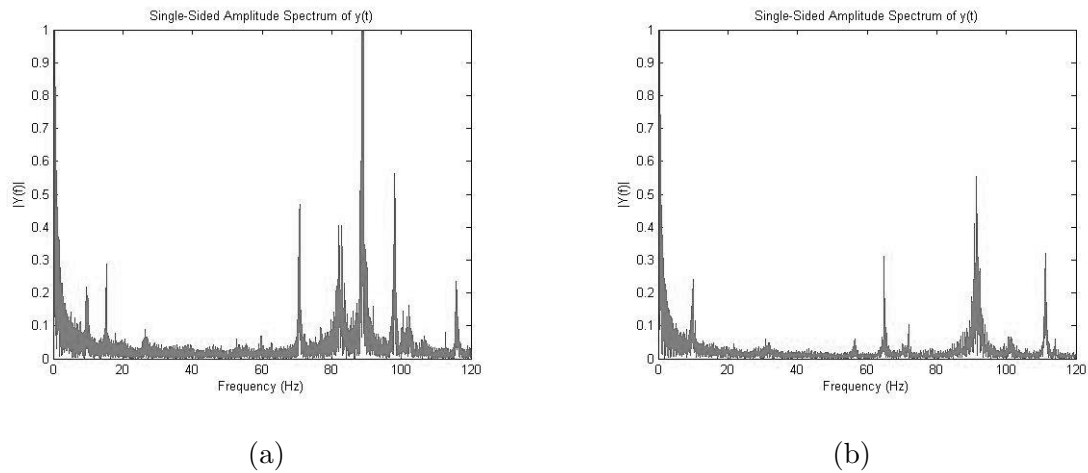
Figure 6.5: FFT of data from position 7 (a), and position 8 (b).

Figure 6.5, shows the FFT of both position seven and position eight. The accelerometers at position seven were placed on the upper 2/5ths of the front bracing tube. Those at position eight were placed near the steering wheel bracket. Position seven shows the highest response at frequency 88.69 hz, which is mode seven. It is interesting to note that in addition to the first few bending modes, this position also picked up many high frequency modes. Position eight also shows a peak at mode eight, at a frequency of 91.52 hz.

Figure 6.6, shows the FFT of position nine, which had the accelerometer placed on the diagonal bracing of the roll halo. The accelerometer was mounted to this tube with ties, not with the heavy accelerometer bracket as was in all the other tests. This was due to the size of the tube it was attached to at this position. Note that the FEA modal analysis specifically for this mode also does not have extra point mass as well. This position should get high responses from the higher modes. This was the case, as mode nine at 108.4 hz had the highest response, and there was also small response from modes four and five.
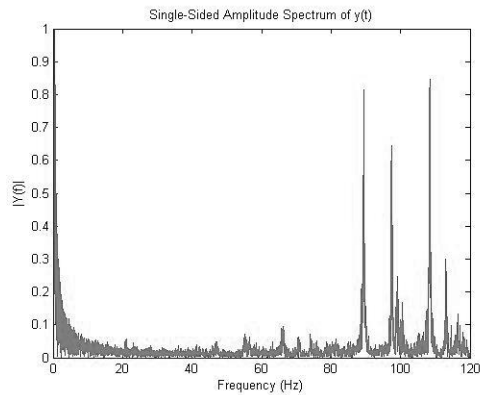
Figure 6.6: FFT of Position 9

The plots of the frequency response data are used to create a table with natural frequencies versus accelerometer position, which the max and min values are provided in Table 6.1. Since the accelerometer and its support bracket represent a mass of 0.6 kg (1.3 lb), the frequency of vibration for certain modes will change, and using the frequency response data the amount of variation for each frequency can be seen. This change happens due an increase in mass for a constant stiffness. The experimental frequency data is compared to the simulated data in the next section.

6.1.2 Modal Analysis of the Simulated Frame

The modal analysis of the simulated frame was be done in several ways, in order to get a range of values that represent valid solutions. Three analyses were done, comparing the formulation of the simulation, the modeling of the masses, and the modeling of the constraints. Comparing the formulation of the simulation involved comparing the frequency results between a lumped mass matrix and a coupled mass matrix. This range of values

62

represents the change in frequency due to different formulations of the mass matrix, and as shown in Table 6.3 the change in frequency is small.

It was necessary to know the effect of adding the mass of the accelerometer bracket to the system. Nine simulated cases were run, in which a point mass representing the accelerometer bracket was placed in a different position corresponding to those in Figure, 6.1. This analysis compares the frequency change by repositioning the accelerometer bracket. As noted in the section above, this bracket is also repositioned in the experimental modal analysis. The maximum and minimum frequencies are shown in Table 6.2. In comparing these two tables to each other, Table 6.1 and Table 6.2, the frequencies of the lowest modes do not match well.

The goal of the final analysis was to determine what effect the assumption of a rigid constraint would have on the frequencies. The table that the frame is connected to is assumed to be rigid, but if that assumption was not valid, the effect had to be known. A simulation was done that included the attachment table as part of the structure, and the result was that the first three natural frequencies dropped frequency significantly. The frequency results are documented in Table 2. Without more modal experiments with different boundary conditions, it is not possible to say that the exclusion of the attachment table is a bad assumption, but it is a possibility. A comparison of the finite element modal solution to the experimental modal solution is shown in Table 6.4.

The experimental frequencies and relative magnitude of each were output by taking
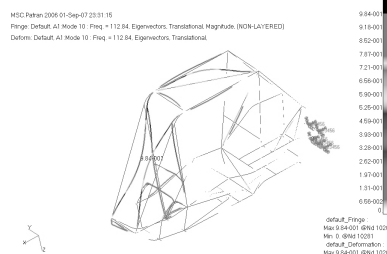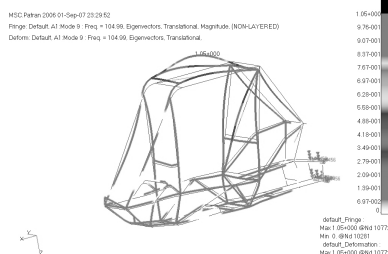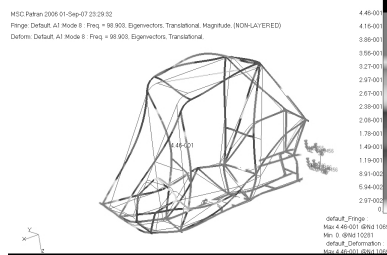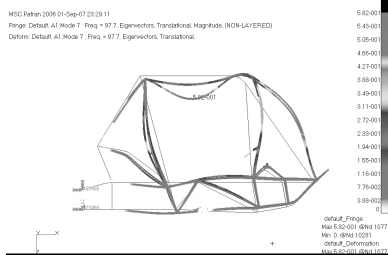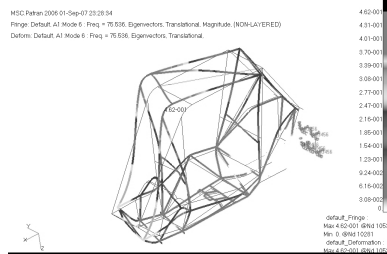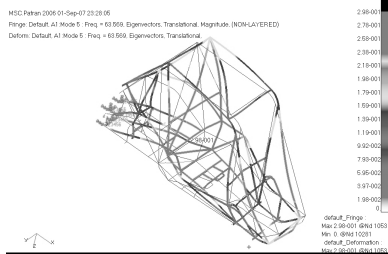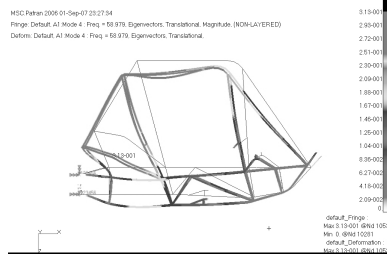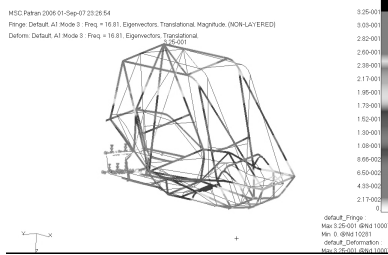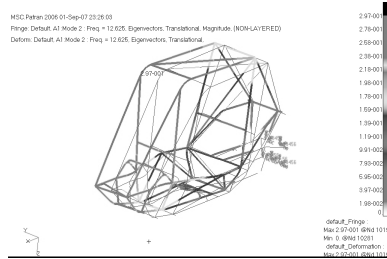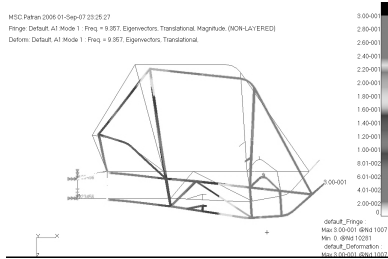
Figure 6.7: Finite Element Modal Solution Fixed at Rear

64

accelerometer data and converting them to Fast Fourier Transforms. A range of frequencies were found for each mode. The frequencies from the MSC.Nastran runs with the bracket in different positions are documented in Table 6.2.

Mode	Max	Min	Delta
1	8.322	7.882	0.44
2	9.991	9.465	0.526
3	15.82	14.75	1.07
4	56.7	53.36	3.34
5	68.34	64.94	3.4
6	72.7	70.71	1.99
7	89.44	88.46	0.98
8	94.32	91.52	2.8
	97.98	96.76	1.22
9	108.5	106.7	1.8
10	113	111.3	1.7

Table 6.1: Table of experimental frequency changes

Without the bracket a lumped run and a coupled run were done to use as a bound. The results of it are shown in Table 6.3. Note that the difference in frequency for the bracketed runs is from 0.22 hertz to 12.12 hertz. The difference between the lumped and coupled with no bracket is 0.0003 hertz to .0628 hertz. The difference between the bracketed runs is at least an order of magnitude larger. Since the bracketed runs are also more realistic to the experiment, they will be used for comparing the results. A comparison of the maximum values and the minimum values of the brackets runs are shown in Table 6.4.

6.2 Dynamic results

The dynamic validation done compared the simulation's seat belt loads and accelerations to those of the experiment. A comparison is made between the forces in the shoulder

Change in frequency due to position of bracket

Mode	Positions						
	a	b	c	d	e	f	g
1	9.12	9.24	9.34	9.33	9.16	9.16	9.22
2	12.34	12.48	12.62	12.60	12.27	12.28	12.39
3	16.60	16.30	16.72	16.79	16.59	16.76	16.77
4	58.90	57.52	57.86	58.39	58.02	58.08	58.55
5	63.03	63.27	63.24	62.40	63.44	62.62	63.33
6	74.72	74.45	75.46	75.48	71.15	73.86	74.74
7	95.48	96.79	97.70	97.08	96.64	85.57	92.41
8	97.48	98.36	98.44	98.88	98.25	90.66	94.56
9	104.72	104.31	104.83	103.70	103.51	99.10	104.27
10	112.53	112.70	112.63	112.79	112.44	104.34	112.52

Mode	Max	Min	Delta
1	9.34	9.12	0.22
2	12.62	12.27	0.35
3	16.79	16.30	0.49
4	58.90	57.52	1.38
5	63.44	62.40	1.04
6	75.48	71.15	4.33
7	97.70	85.57	12.12
8	98.88	90.66	8.23
9	104.83	99.10	5.72
10	112.79	104.34	8.45

Table 6.2: Table of simulated bracketed runs

	Lumped Vs Coupled				
Mode	Lumped	Coupled	Mode	Delta
1	9.36	9.36	1	0.0011
2	12.62	12.63	2	0.0015
3	16.80	16.81	3	0.0087
4	58.92	58.98	4	0.0628
5	63.55	63.57	5	0.0157
6	75.48	75.54	6	0.0573
7	97.71	97.70	7	-0.0078
8	98.85	98.90	8	0.0567
9	105.00	104.99	9	-0.0044
10	112.84	112.84	10	0.0003

Table 6.3: Table of Lumped Frequencies vs. Coupled Frequencies

	Experimental		Simulated		Sim - Accl Brkt		Sim - w/
Mode	Max	Min	Lumped	Coupled	Max	Min	table
1	8.32	7.88	9.36	9.36	9.34	9.12	6.48
2	9.99	9.47	12.62	12.63	12.62	12.27	9.89
3	15.82	14.75	16.80	16.81	16.79	16.30	15.81
4	56.70	53.36	58.92	58.98	58.90	57.52	56.31
5	68.34	64.94	63.55	63.57	63.44	62.40	66.89
6	72.70	70.71	75.48	75.54	75.48	71.15	75.10
7	89.44	88.46	97.71	97.70	97.70	85.57	91.00
8	97.98	96.76	98.85	98.90	98.88	90.66	98.91
9	108.50	106.70	105.00	104.99	104.83	99.10	107.72
10	113.00	111.30	112.84	112.84	112.79	104.34	112.14

Table 6.4: Table of Experimental Frequencies vs. Nastran Frequencies

belt and lap belt, the acceleration of the head and chest, and the overall body motion. The force input into the simulation was a reduced set of the experimentally determined load. An example of a typical load is shown in Figure 6.8 (a), with a detailed view shown in Figure 6.8 (b). The values for the loading were input into MSC.Dytran in a tabular form and are plotted in Figure ??.
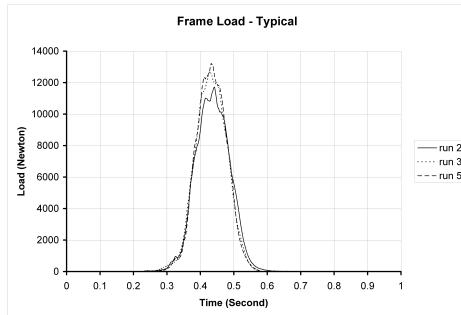
(a)
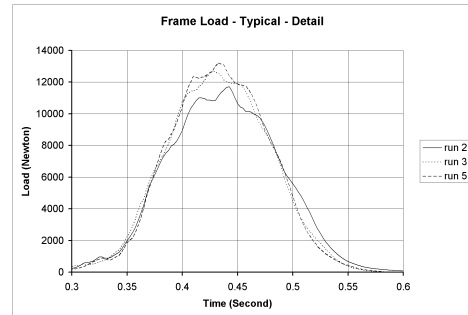
(b)
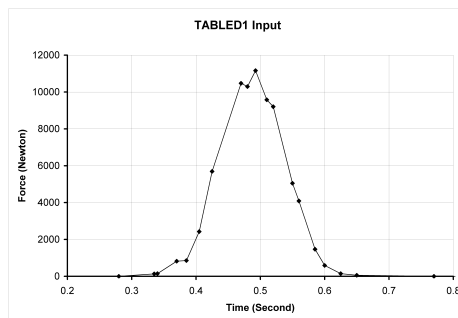
(c)

Figure 6.8: Typical load history of the frame load cell (a), and a detailed view (b); TABLED1 load (c).

6.2.1 Low-Friction Belt Experiment and Simulation
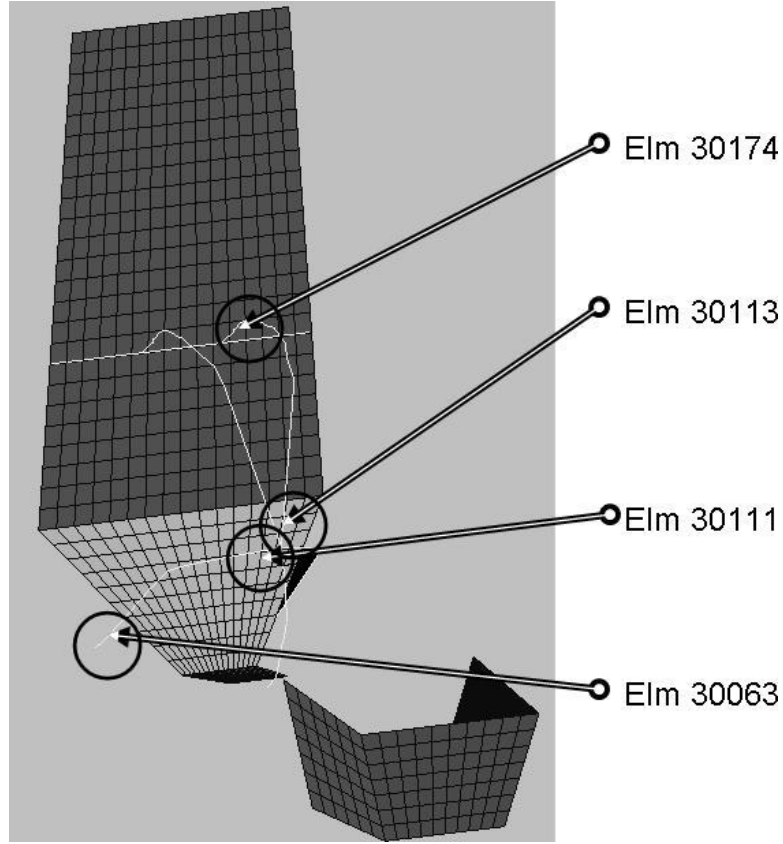
Figure 6.9: The FEM element position

The locations of the load cells in the experiment are shown in Figure 6.9; while the locations of the elements that represent those load cells are shown in Figure 6.10. Note that four elements are depicted in the previous figures so that the difference in forces due to friction on the body can be shown. For clarity, all plots show three cases where the peak value was relatively high, average, and low. The effects of belt pretension are shown in the Appendix 2. The results from the experiments, will be shown in the following order: experiments with zero friction, loose belts, and tight belts. Detailing the conditions in each
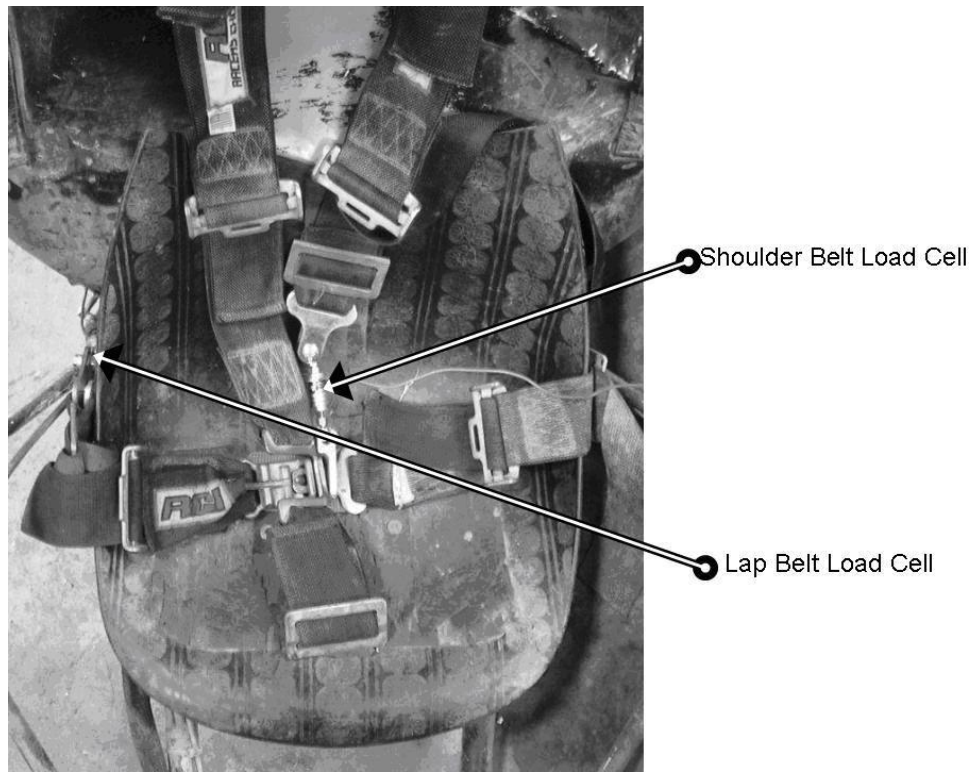
Figure 6.10: Load cell physical location

cases, the zero friction case represents an effort to reduce the effects of friction as much as possible. This was done by placing layers of wax paper between the belt and the person and the seat and the person as shown in Figure 6.11. In this experiment the belts were tight with a preload in the shoulder belts beginning at 25 Newtons. The loose belt case represented the average driver in the vehicle, restrained with belts that have no preload. In this way, the body has to move further before engaging the belts. The tight belt case represented a restrained driver with the most possible preload. Although the amount of preload fell as the belts were strained, the preload began at a load of 133 N for the first case, and fell to 56 N for the last three cases. The results of the low friction belt experiment show a multi-peak

Figure 6.11: Detail of wax paper to provide low friction surface

response that is repeatable and is specifically a consequence of the low friction. For this case, comparing the experiment with the simulation shows good agreement in magnitude,

but little agreement in shape. In particular, the multi-peak affect shown in the plots of the experiment should show up in the simulation. It is unknown why the shoulder belt had a high frequency oscillation. For the same case, the lap seat belt had no such artifact, most likely due to it being well constrained between the torso and the leg.

The lap belts show a very clean response in the experiment, with a maximum magnitude of 600 N (134 lb). The shape of the loading is very different from the shoulder belts, and is very similar to the shape of the cases with friction. This may be because the lap belt had much greater contact with the body than the shoulder belts did. Even with the wax paper to reduce friction, the contact did not allow the loading to change. A secondary force peak is noticeable approximately 200 msec after the main loading pulse. This second pulse is also in the experiment and represents the occupant oscillating between the belts and the seat.

6.2.2 Low Tension Belt Experiment and Simulation

The low tension experiments represent runs where the belts had no initial force on them. These experiments are shown in Figure 6.14. The shoulder load cell had a maximum force of 500 N (112 lb), and the simulated belt force had a maximum of 600 N (134 lb). For the shoulder belt loads, the simulation had a very similar pulse shape to the experiment, however it was elongated by 100 msec. Both results show a plateau of 25 msec before the maximum peak. For the lap belt loads shown in Figure 6.15 neither the magnitude of the load nor the shape of the load match.
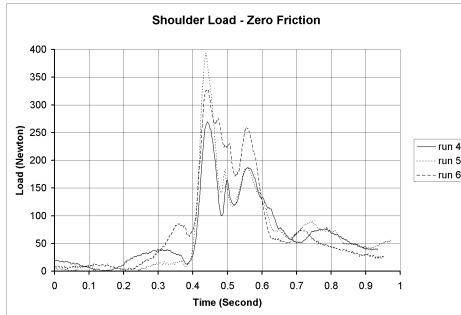
(a)
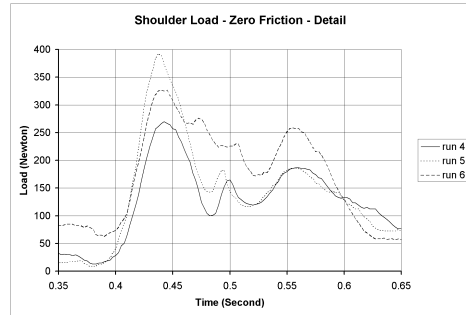
(b)
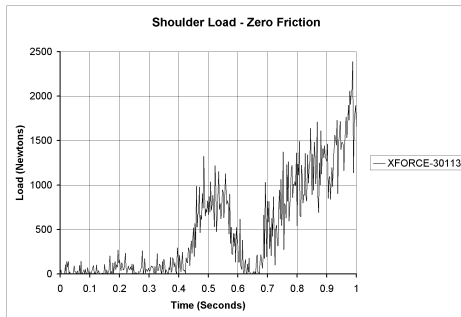
(c)
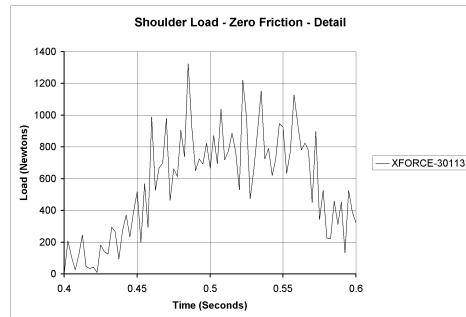
(d)

Figure 6.12: The zero-friction, shoulder belt results for the Experiment (a), with detail (b), and the Simulation (c), with detail (d).
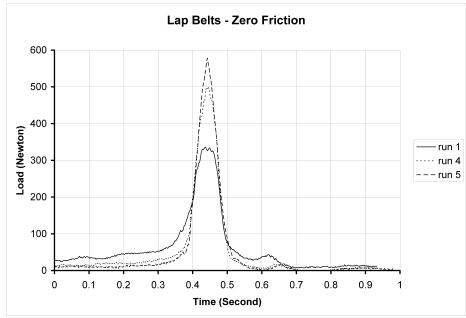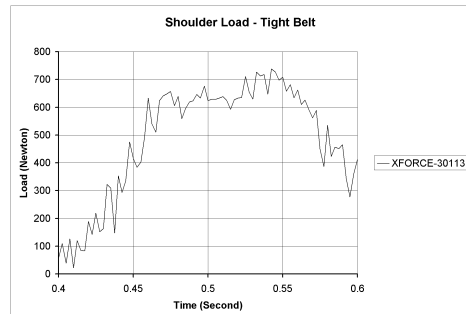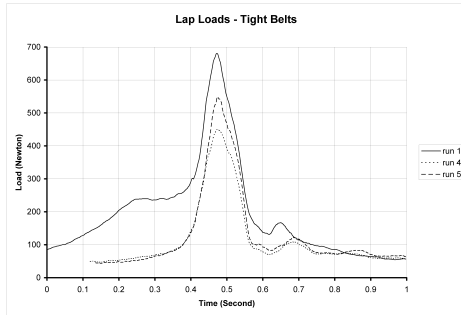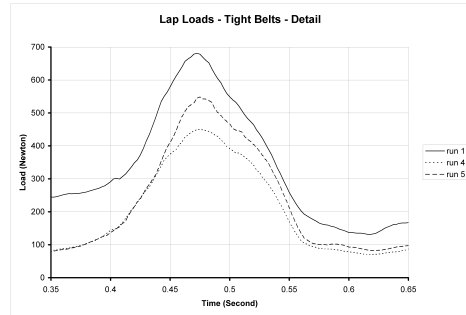
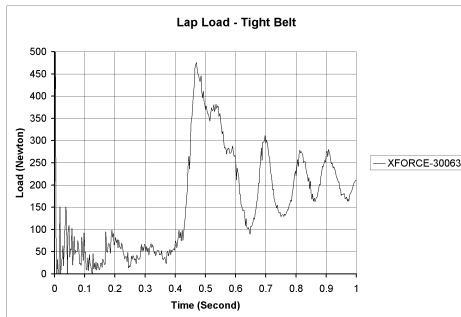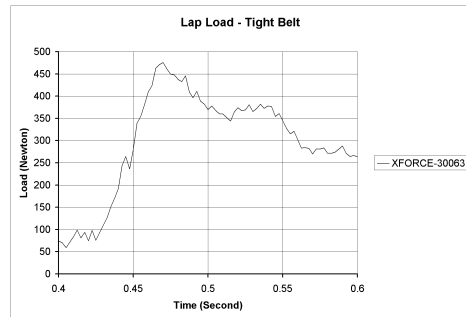(a)
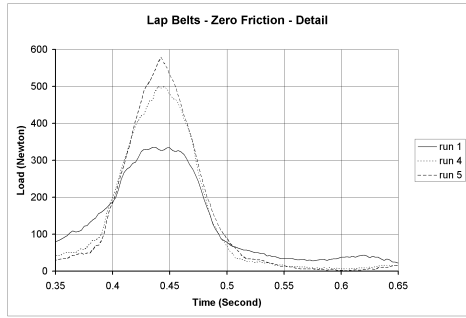
(b)
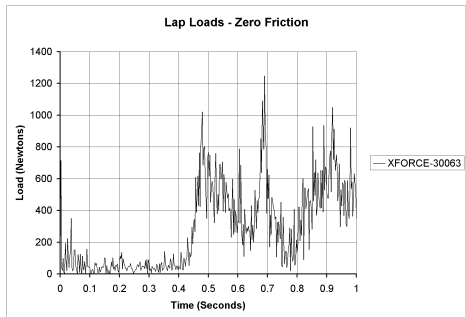
(c)
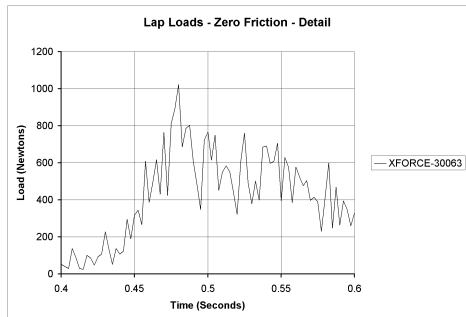
(d)

Figure 6.13: The zero-friction, lap belt results for the Experiment (a), with detail (b), and the Simulation (c), with detail (d).
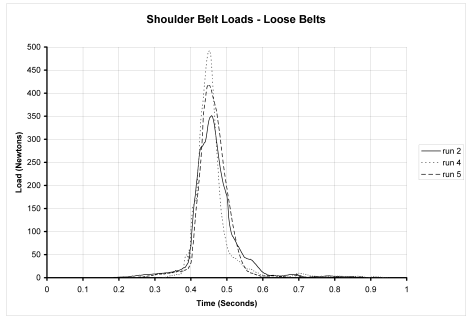
(a)
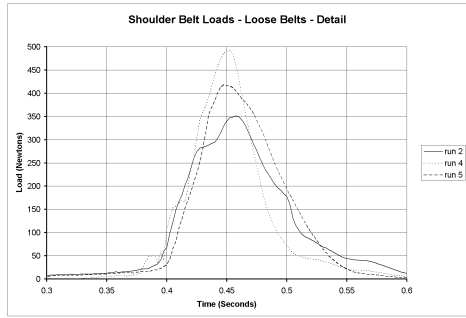
(b)
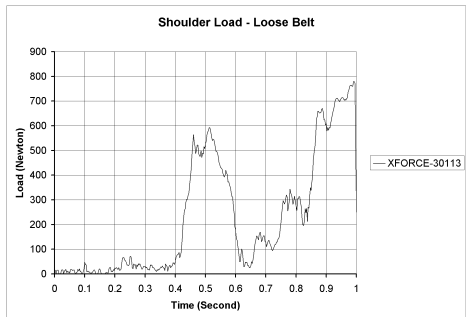
(c)
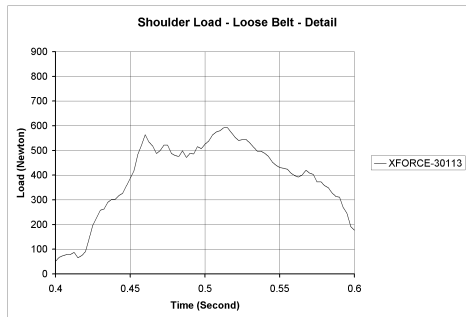
(d)

Figure 6.14: The low tension, shoulder belt results for the Experiment (a), with detail (b), and the Simulation (c), with detail (d).
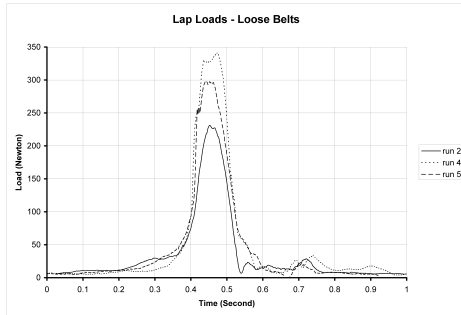
(a)
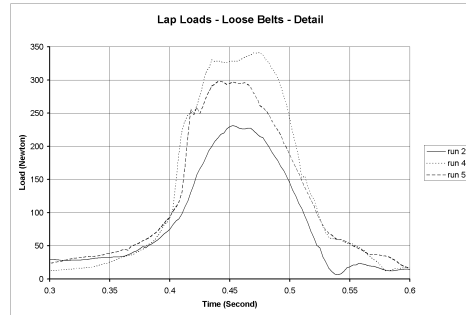
(b)
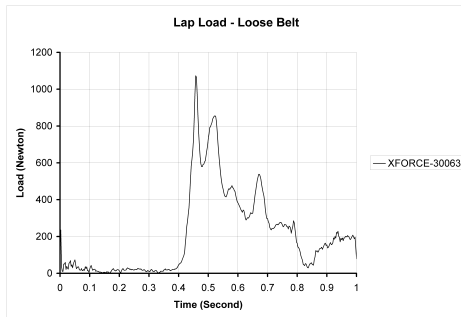
(c)
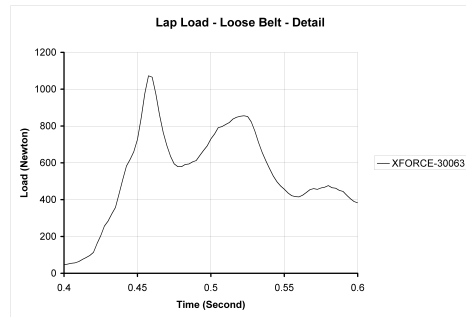
(d)

Figure 6.15: The low tension, lap belt results for the Experiment (a), with detail (b), and the Simulation (c), with detail (d).

6.2.3   High tension belt experiment and simulation

The high tension belts had an initial load of around 75 N (17 lb). As shown in Figure 6.16, the experimental shoulder belt loads have a duration of blank and have a peak magnitude of approximately 325 Newtons (73 lbf). The simulation results have a peak magnitude of over 600 N, or double the recorded loads in the experiment. In the experimental results, there are smaller peaks at approximately 600 and 800 msec. This result is duplicated in the simulation, whereupon it shows peaks at 700 and 800 msec, these peaks are spaced much closer together. A possible explanation for this result can be the interaction of the human with the system, since the human being is an active controller it is possible that the body motion was being damped, which would extend the time of the secondary peaks. Another explanation is that there is strong interaction between the seat contact and the belt contact on the body. Since the body is rigid in this simulation, the belts and seat must take up all of the deformation, thus making the frequency of the contact higher. The lap belt loading shows a much closer result than the other belts. Comparing the simulation to the experiment, both in Figure 6.17, the simulation is within the maximum and minimum values recorded in the experiment at 450 Newtons (100 lbf). The general shapes of the two are similar, with both having an abrupt increase to maximum load, followed by a more gradual unloading. The body induced oscillating is also present.

6.2.4   Effect of friction coefficient on seat

The friction between the seat and the person is unknown in every case except the low friction case, where wax paper separated the body from the seat. In all other cases, the friction was determined by contact between cloth and plastic. A simulation was run to
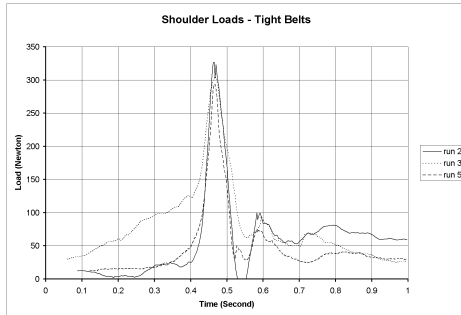
(a)
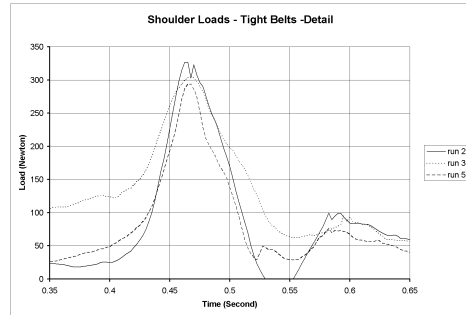
(b)
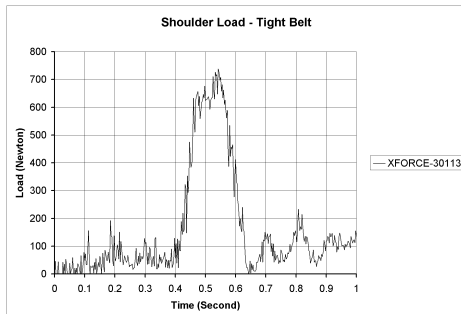
(c)

(d)

Figure 6.16: The high tension, lap belt results for the Experiment (a), with detail (b), and the Simulation (c), with detail (d).

(a)

(b)


(c)


(d)

Figure 6.17: The high tension, lap belt results for the Experiment (a), with detail (b), and the Simulation (c), with detail (d).

analyze the effect of increasing the seat coefficient of friction from .12 to .5. In early work with friction between the belts and the body, it was found that between .20 and .50 friction, the contacts "locked," which means they maintained a high contact force when one was not necessary, see Appendix **??**. In maintaining the belt friction constant and increasing the seat friction, the same effect of "locking," happened. In this case, the peak magnitude of the force also went down compared to the other data sets. Thus friction does play an important role in determining the belt loads, so this is a place where the data was insufficient.
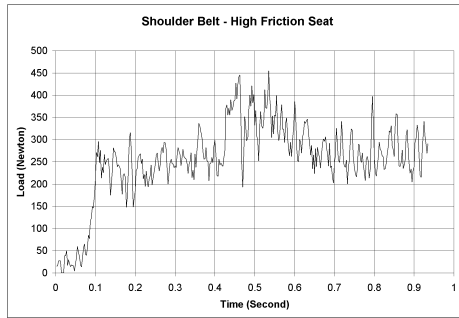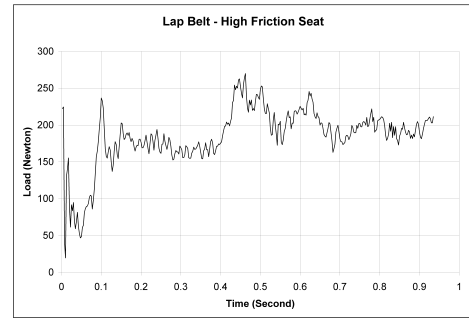
(a)   (b)

Figure 6.18: The effect of seat friction on lap belt loads (a), and shoulder belt loads (b).

6.2.5   Head acceleration

The acceleration data for the occupant's head is separated into three groups, corresponding to the three cases of the belts: low friction, low tension, and high tension. The response of the head will be less exact due to the rotation of the accelerometer, but the order of magnitude of the results should be similar. For the low friction case, the peak accelerations in the experiment were approximately 6 G's in deceleration. The simulation

over-approximates this number by 1G, however the shape of the acceleration pulse well matches the experimental results. It matches in terms of the duration of the pulse at 200 msec. The result of approximating the neck as a spring is the oscillation shown in Figure 6.19, part (c). Since the human body's head is actively controlled, little oscillation is shown. The accelerations in the Z-direction show similar shapes, however there is an unknown issue with the simulation history. The acceleration history goes positive for a short period, which probably indicates that the contact routine had trouble converging on a solution and resulted in a positive force.

For the case of low tension belts, the simulation over predicts the magnitude of the acceleration of the head by 2 G's. Although the plots are very similar to the low friction plots in terms of the overall shape, there is a discrepancy. The smaller peak before the larger one in the experimental data was assumed to be a larger magnitude response of the oscillation that was in the experimental data. However, comparing Figures 6.21 and 6.22, both simulation plots show an opposite response beginning at time 460 msec, showing that this is an artifact of the simulation, and not an agreement.

The head accelerations for the high tension belt case show roughly the same magnitude and shape as the previous cases. This would seem to indicate the belt tension does not have a strong effect on head accelerations under these conditions. In this case, the simulation shows no artificial peak like in the previous two cases, and shows better agreement in the shape of the data. Both the simulation data and the experimental data show a plateau immediately preceding the highest peak, and an inflection soon after the peak.
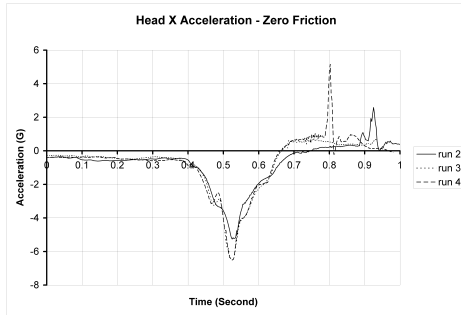
(a)
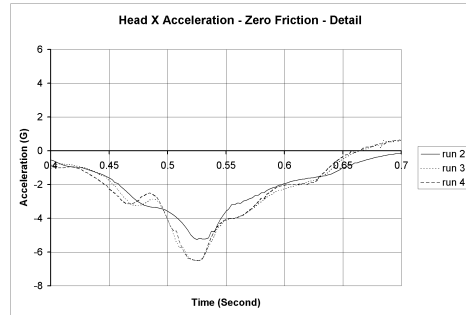
(b)
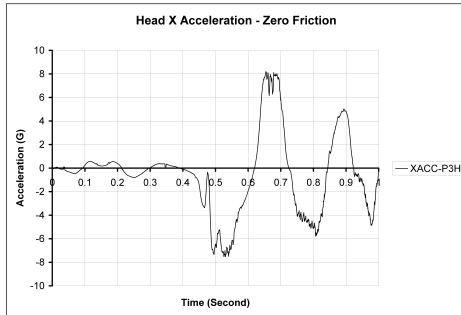
(c)
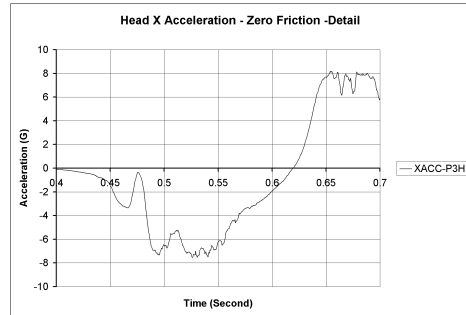
(d)

Figure 6.19: The zero-friction, head X-acceleration results for the Experiment (a), with detail (b), and the Simulation (c), with detail (d).
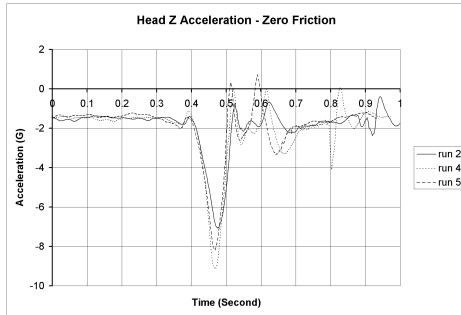
(a)
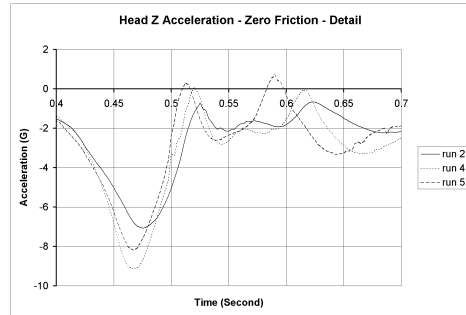
(b)
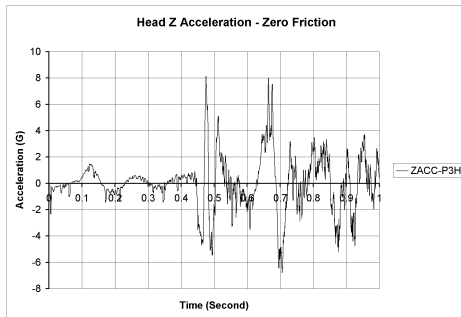
(c)
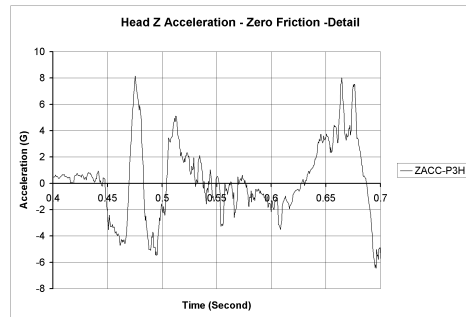
(d)

Figure 6.20: The zero-friction, head Z-acceleration results for the Experiment (a), with detail (b), and the Simulation (c), with detail (d).
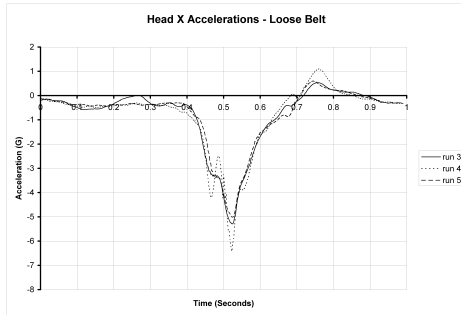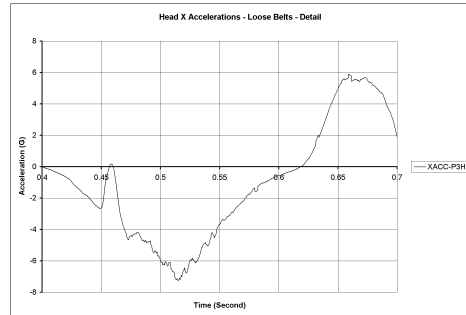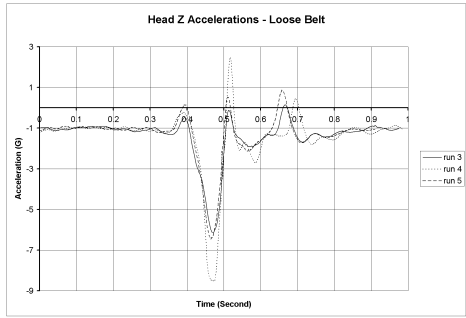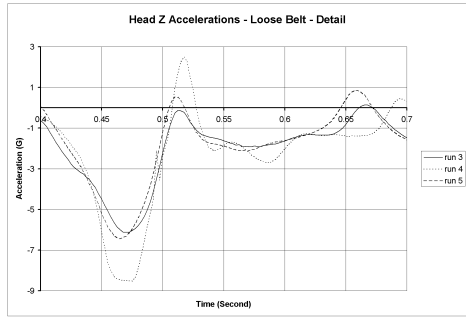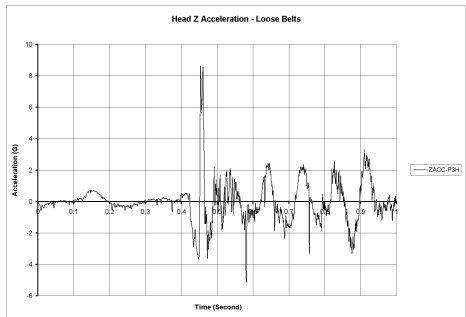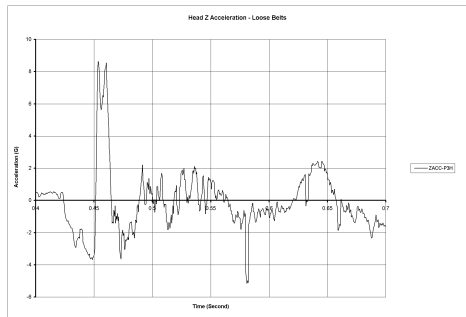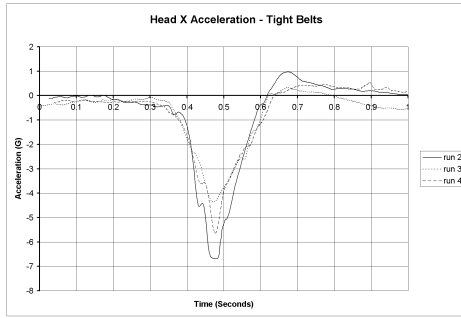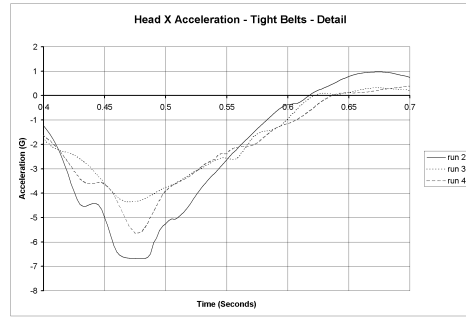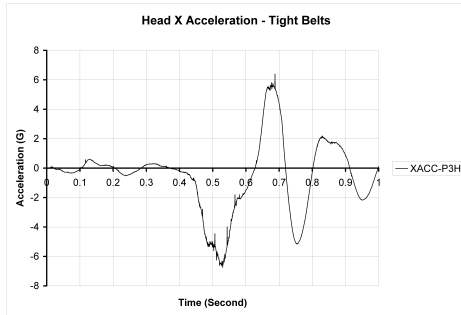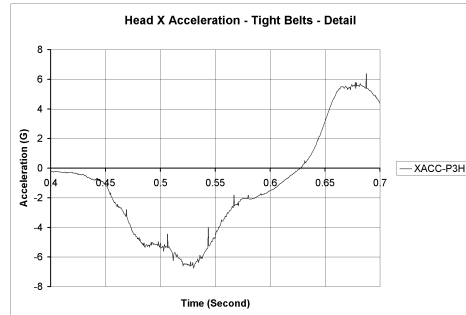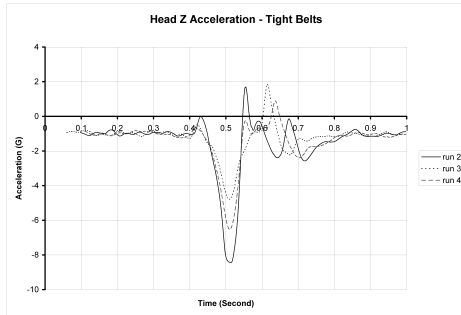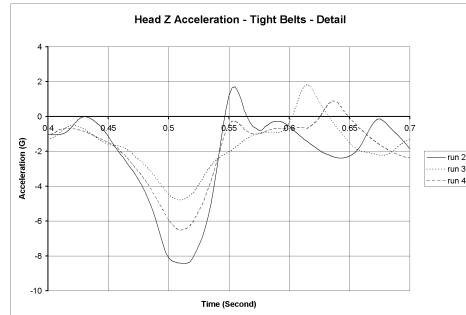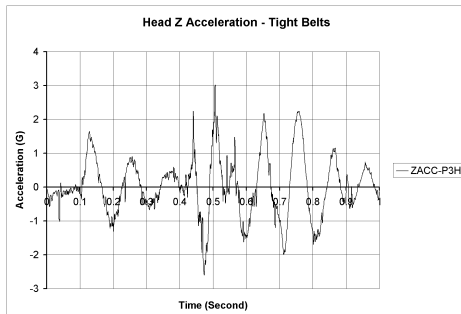
(a)
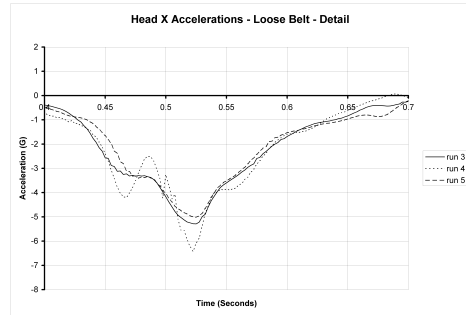
(b)
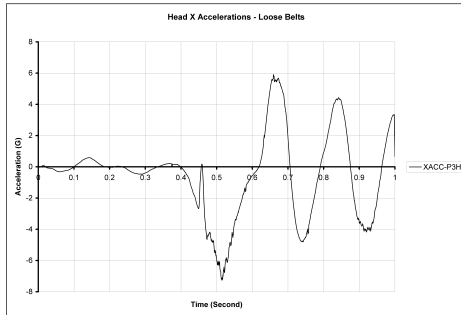
(c)

(d)

Figure 6.21: The low tension, head X-acceleration results for the Experiment (a), with detail (b), and the Simulation (c), with detail (d).
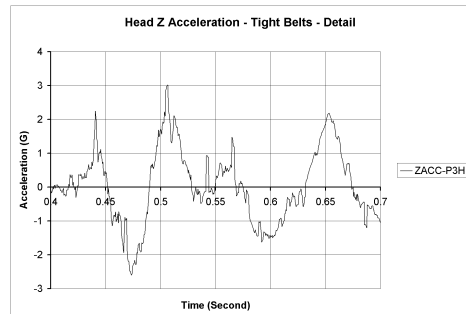
84

(a)

(b)

(c)

(d)

Figure 6.22: The low tension, head Z-acceleration results for the Experiment (a), with detail (b), and the Simulation (c), with detail (d).

(a)

(b)

(c)

(d)

Figure 6.23: The high tension, head X-acceleration results for the Experiment (a), with detail (b), and the Simulation (c), with detail (d).

(a)

(b)

(c)

(d)

Figure 6.24: The high tension, head Z-acceleration results for the Experiment (a), with detail (b), and the Simulation (c), with detail (d).
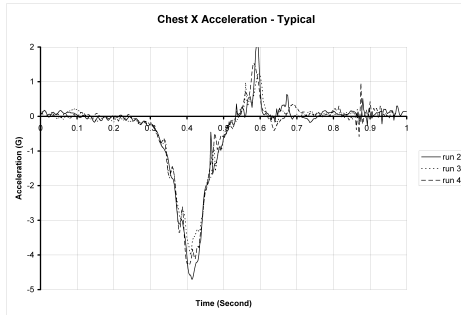
6.2.6 Chest accelerations

The chest acceleration data provided is for the typical case. In the X direction, the accelerations are over-predicted by the simulation by 1G, and the duration is similar between the experiment and the simulation. A large spike in the data is attributed to contact problems. In the Z direction, the acceleration is over predicted by approximately 4G's, and has a similar spike in it that is attributed to contact problems.

6.2.7 Motion of the vehicle

The motion of the frame in the Z direction will be ignored. This is due to a physical difference between the experiment and the simulation. The experiment had contact between the tires and the ground, which are similar to springs and dampers between the ground and the frame. The simulation has a single point constraint in the Z direction at the four shock points, as well as constraints in the Y direction at all the suspension attach points. Note the results for the experiment in the Z direction have upper and lower bounds of 1.5 to -1.5 G, signifying that little major acceleration took place in the up and down direction.

6.2.8 Gross Body Motion

The gross motion of the human body in the experiment and the simulation should match well for the simulation to be valid. The motion of the body is consistent amongst all the simulated runs, even if the results of the seat belt loads are not. Motion capture was not a priority, so there are limited pictures in which to use for comparison of the simulation and the experimental occupant. There are three sets of pictures for both the simulation and the experimental occupant, shown in Figure 6.31.
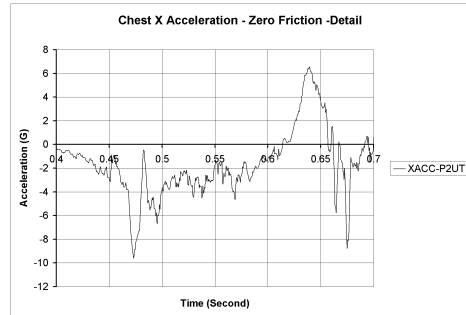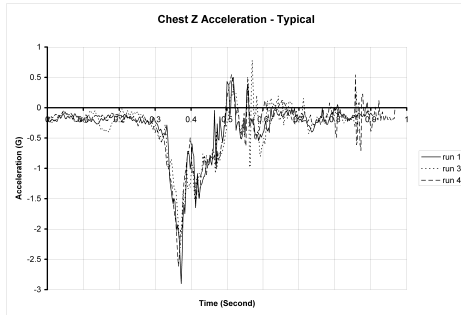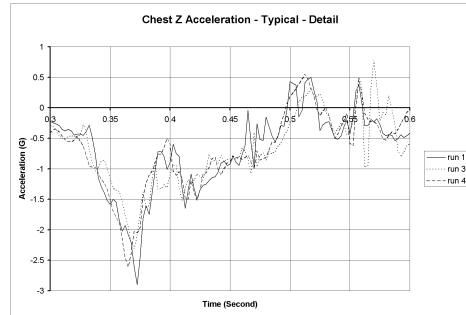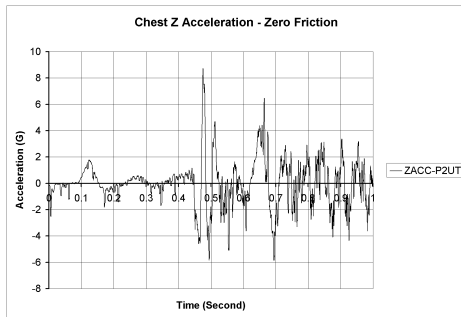
(a)
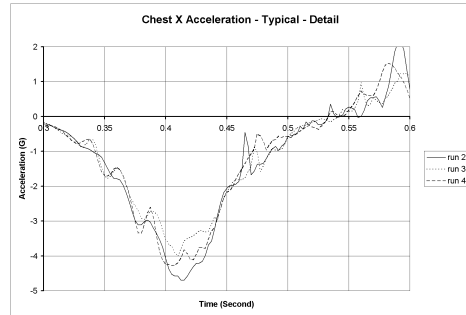
(b)
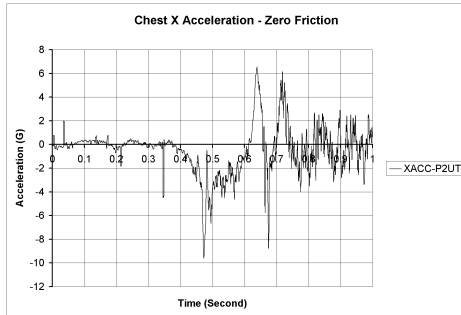
(c)

(d)

Figure 6.25: Typical chest X-acceleration results for the Experiment (a), with detail (b), and the Simulation (c), with detail (d).
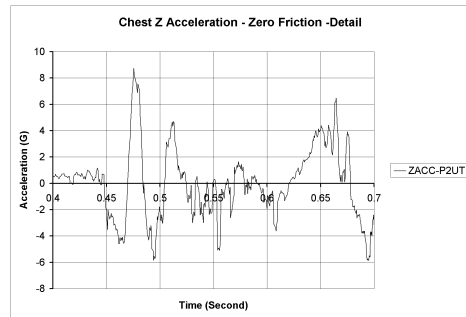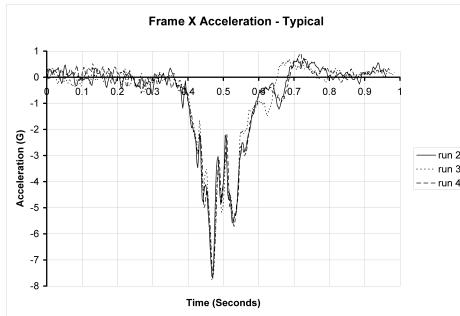
(a)

(b)

(c)
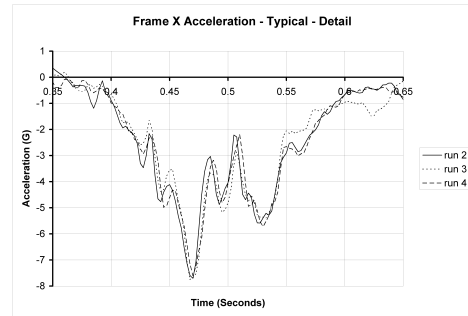

(d)

Figure 6.26: Typical chest Z-acceleration results for the Experiment (a), with detail (b), and the Simulation (c), with detail (d).

(c)   (d)

Figure 6.27: Plot of acceleration vs. time from accelerometer (a), with detail (b).
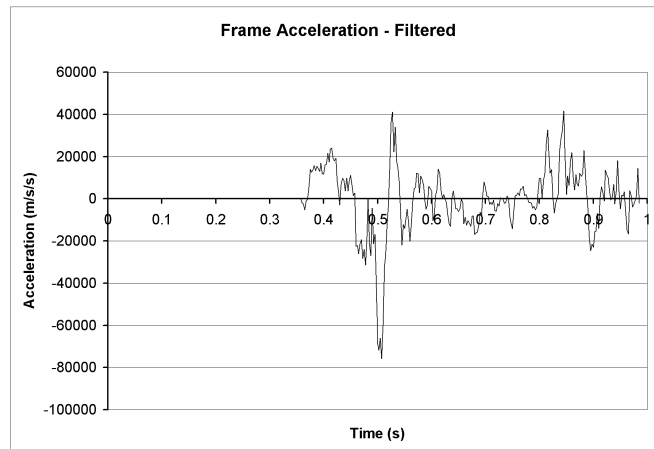

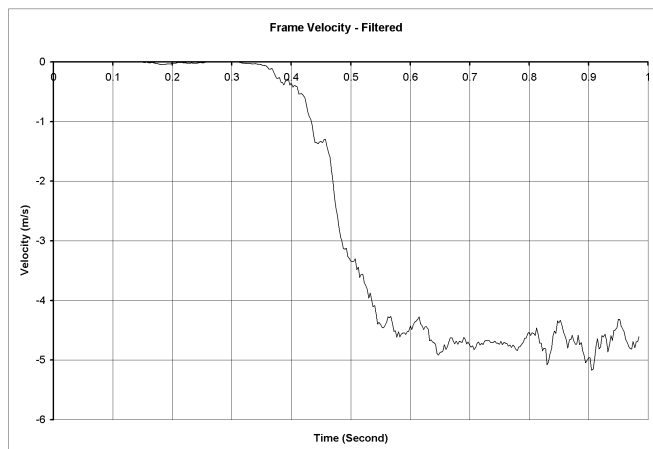Figure 6.28: Plot of acceleration vs. time for point on vehicle frame.

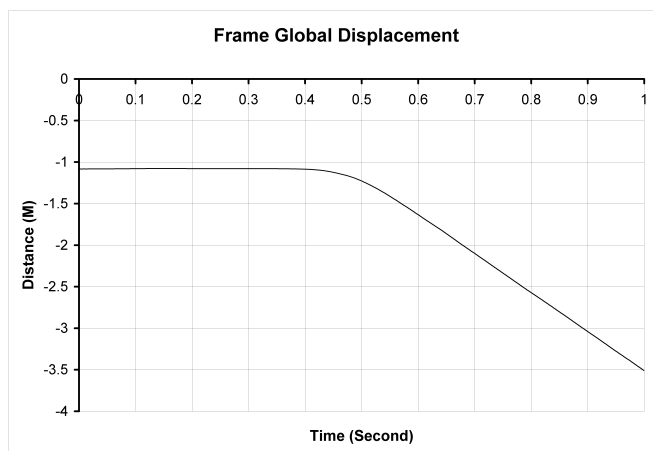Figure 6.29: Plot of velocity vs. time for point on vehicle frame.


Figure 6.30: Plot of position vs. time for point on vehicle frame.

The first set of pictures shows the unloaded cases for both. The occupant in the experiment has a different arm position than the dummy in the simulation. In both the simulation and the experiment, the occupants are resting flush against the firewall of the vehicle. In the second set of pictures, the acceleration is building up to it's peak. Both bodies show movement away from the firewall, a downwards pitch to the head, and motion of the arms. The head movement shows how the neck allows the head to translate forward somewhat before a significant downward pitch of the head. The arms have moved upwards in both simulations, however in different ways. In the simulation, the arms have no contact interaction with the body and are allowed to pass through the body. As such, the arms begin translating forward and rotating upwards, very different from the simulation. In the experiment, the arms are much better constrained by the driver, but also translate forward and upwards. This can be seen by comparing the first two sets of experimental photos, by which it can be shown that in the first set, there is a triangular gap between the arm and the leg at the elbow; in the second set, this gap is gone. Also notice that the wrists in the experimental photo have changed position, which signifies that the arm is sliding up the leg. Note that in the experiments, the driver was conscious and was thus actively controlling the motion of the body. The arms were constrained by holding the steering wheel. In the simulation, the arms had no such constraint, and although none was desired, the closest correlation would have been to use the ATB input file to provide a very high locking force to keep the joint from rotating [7]. In the third set of pictures, the experiment shows that the body has regained contact with the firewall, the head has a large downward pitch, and the arms have traversed around three inches up the leg (based on the movement of the

watch). The hands no longer contact the steering wheel, further signifying the translation of the arm up the leg.
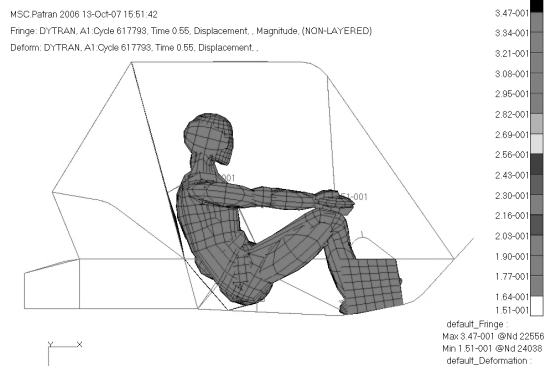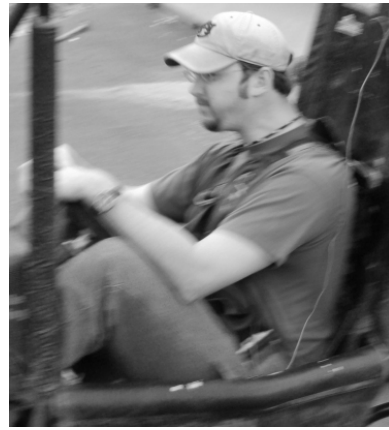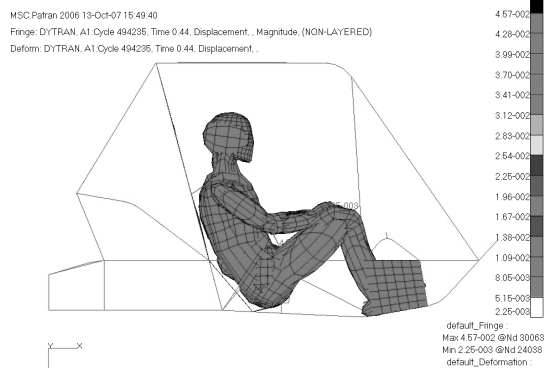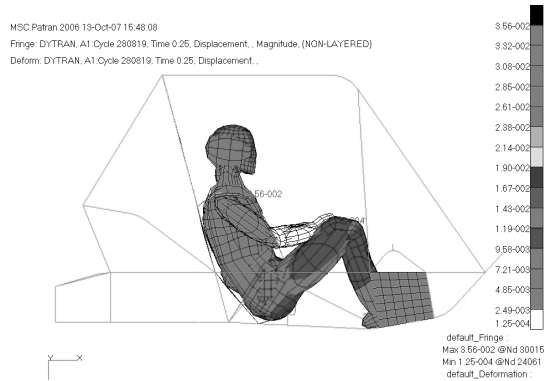
Figure 6.31: Occupant response Simulation (a) and Experiment (b)

95

Conclusions

The occupant and vehicle interaction simulation works well for this specific load case. This simulation poorly matches the magnitude of the loads, in general it over-approximates them, but the shape of the loading is matched well. With the lack of fidelity in the seat, and modeling issues with the human body, there are several reasons the model could have an error in magnitude. The model presented is a way to assess whether changes in a structure can better protect the human body. It is a way to effect changes in design of the frame structure and see the changes in a relative fashion.

CHAPTER 8

FUTURE WORK

This computer simulation has been validated for a specific case. To make it more robust, further validations must be made to detail an operational envelope in which the simulation is accurate. Further work with a person would involve matching gross body motion in the simulation with a more complex event, like jumping an obstacle. Using load-cells to record the suspension data (the load into the frame), the model could re-create the jump and the gross body motion could be compared. Other validation would have to be done without a person due to the high accelerations, but with the mass added to the system in another fashion. These validations would include accelerating the Baja SAE vehicle to a known speed, and impacting it into a rigid obstacle of known shape like a tree or concrete divider. In this way the material properties of steel can be modified such that the simulation has the same deformations as the experiment. The occupant and vehicle interaction model opens the door to many different fields of study. Study into frame design, occupant protection, restraint harness design (seat and seat belts), energy-absorbing front bumpers, frame failure, and more.

Bibliography

[1] Digges, K. H., "Recent Improvements in Occupant Crash Simulation Capabilities of the CVS/ATB Model," SAE Document: 880655.

[2] Doebelin, E. O., $Engineering Experimentation : Planning, Execution, Reporting$. New York:Mc-Graw-Hill, Inc., 1995.

[3] Fasanella, E. L., and Jackson, K. E., "Best Practices for Crash Modeling and Simulation," ARL-TR-2849.

[4] Grimes, W. D., "Using ATB in Collision Reconstruction," SAE Document: 950131.

[5] Huanining, C., Rizer, A. L., and Obergefell, L. A., "Pickup Truck Rollover Accident Reconstruction Using the ATB Model," SAE Document: 950133.

[6] Huanining, C., Rizer, A. L., and Obergefell, L. A., "ATB Model Simulation of a Rollover Accident with Occupant Ejection," SAE Document: 950134.

[7] Huanining, C., Rizer, A. L., and Obergefell, L. A., "Articulated Total Body Model Version V User's Manual," ASC-98-0807.

[8] Huebner, K. H., Dewhirst, D. L., Smith, D. E., and Byrom, T. G., $The Finite Element Method for Engineers$. Fourth Edition. New York: John Wiley & Sons, Inc., 2001.

[9] "Input Description For the Articulated Total Body Model ATB-V.1," December 1998.

[10] "www.mathworks.com," MATLAB function reference - Fast Fourier Transform, http://www.mathworks.com/access/helpdesk/help/techdoc/ref/fft.html, 2007.

[11] Meirovitch, L., $Fundamentals of Vibrations$. New York: McGraw-Hill, 2001.

[12] $MSC.Dytran©2005r3, User's Guide$. MSC.Software Corporation, 2006.

[13] Owens, A. T., Jarmulowicz, M. D., and Jones, P. D., "Structural Considerations of a Baja SAE Frame." SAE Document: 2006-01-3626

[14] Pellettiere, J. A., Huaining, C., and Rizer, A. L., "The Development of GEBOD Version V," Presentation.

[15] Przemieniecki, J. S., $Theory of Matrix Structural Analysis$. New York:Dover Publications, Inc., 1968.

[16] da Silva, M. M., de Oliveria, L. P. R., Neto, A. C., and Varoto, P. S., "An Experimental Investigation on the Modal Characteristics of an Off-Road Competition Vehicle Chassis." SAE Document: 2003-01-3689.

[17] Sitton, G., $MSC.Nastran, Version 69, Basic Dynamic Analysis User's Guide$. MacNeal-Schwendler Corporation, 1997.

[18] Smith, J. A., Rizer, A. L., and Obergefell, L. A., "Predictive Simulation of Restrained Occupant Dynamics in Vehicle Rollovers," SAE Document: 930887.

[19] Trefethen, L. N., and Bau, D. III, $Numerical Linear Algebra$. Philadelphia: Society for Industrial and Applied Mathematics, 1997.

.1 Contact Definition

```
$ Head and Frame Contact
CONTACT,5,GRID,SURF,11011,21050,0.12,0.12,1.0,+
+,V4,TOP,SLIDE,,0.1,0.1,,SLAVE,+
+,,,DISTANCE,0.1,,0.2,,,+
+,.0001,,,,,,,,+
+,,,,,,,,,+
+,
```

Table 1: Contact card in MSC.Dytran

.2 MATLAB Fast Fourier Transform

```
Fs = 1000;                      % Sampling frequency

T = 1/Fs;                       % Sample time

L = 1000;                       % Length of signal

t = (0:L-1)*T;                  % Time vector


NFFT = 2\^nextpow2(L);          % Next power of 2 from length of y

Y = fft(y,NFFT)/L;

f = Fs/2*linspace(0,1,NFFT/2);


% Plot single-sided amplitude spectrum.

plot(f,2*abs(Y(1:NFFT/2)))

title('Single-Sided Amplitude Spectrum of y(t)')

xlabel('Frequency (Hz)')

ylabel('|Y(f)|')
```
 1984-2007 The MathWorks, Inc.

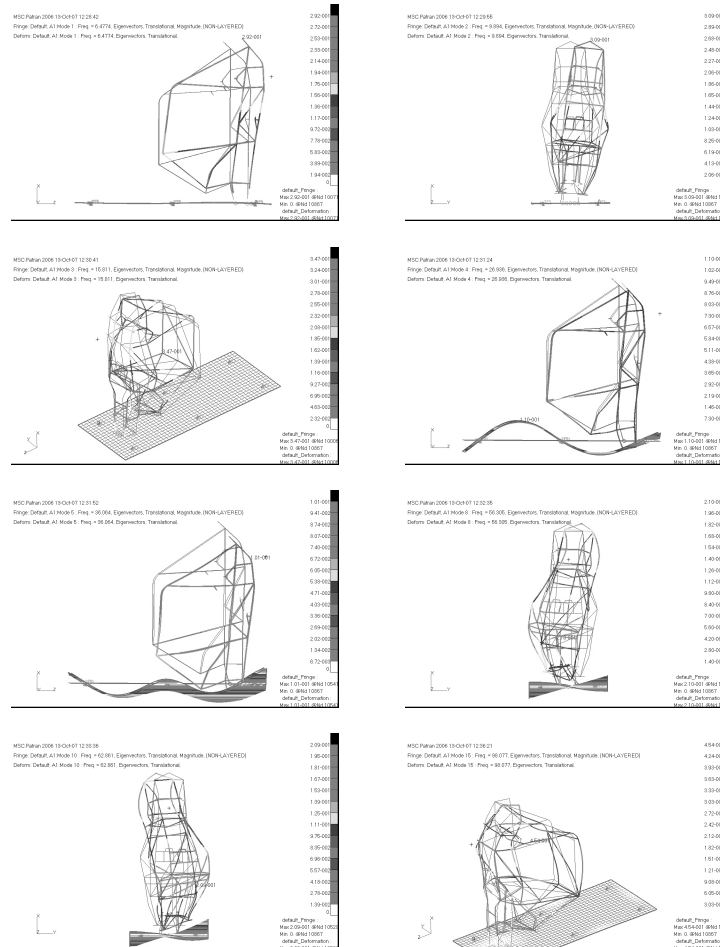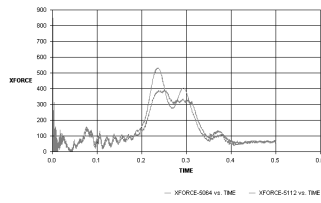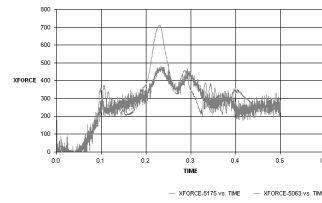## .3 Modal solution with Table

Figure 1: Finite Element Modal Solution Including Table
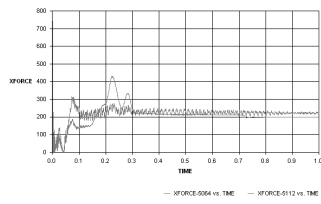
.4 Effects of seat belt friction

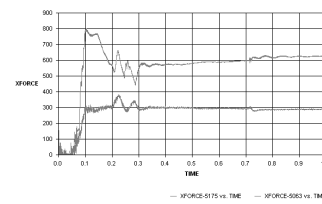
(a)

(b)

(c)

(d)

Figure 2: Belt forces: lower belts .20 (a), upper belts .20 (b), lower belts .50 (c), upper belts .50 (d).

table modal solution		Modes that match between the table and rigid solutions				
mode	frequecy	mode	table freq	rigid freq	diff	% diff
1	6.48	pitch	6.48	9.36	-2.88	-30.77%
2	9.89	yaw	9.85	12.63	-2.78	-21.99%
3	15.81	torsion	15.81	16.81	-1.00	-5.94%
4	26.94	losenging	62.86	63.57	-0.71	-1.11%
5	36.06	halo yaw	75.10	75.54	-0.44	-0.58%
6	44.35	halo pitch	98.91	97.70	1.21	1.24%
7	47.48	halo diag	104.49	104.99	-0.50	-0.48%
8	56.31					
10	62.86					
11	66.89					
12	75.10					
13	76.10					
14	91.00					
16	98.91					
17	104.49					
18	107.72					
19	112.14					
20	113.71					
21	114.31					
22	119.75					

Table 2: Frequencies of Modal analysis with table included in boundary condition

1987